Study of Thermoelectric Behavior of some Double and Triple half-Heuslers

A Thesis

submitted to
Indian Institute of Science Education and Research Pune
in partial fulfilment of the requirements for the
BS-MS Dual Degree Programme

by

S.S.Vishak

Indian Institute of Science Education and Research Pune
Dr. Homi Bhabha Road,
Pashan, Pune 411008, INDIA.

April, 2024

Supervisor: Prof. Surjeet Singh

Certificate

This is to certify that this dissertation entitled "Study of Thermoelectric Behavior of some Double and Triple half-Heuslers" towards the partial fulfilment of the BS-MS dual degree programme at the Indian Institute of Science Education and Research, Pune represents study/work carried out by S.S.Vishak at Indian Institute of Science Education and Research, Pune, under the supervision of Prof. Surjeet Singh, Department of Physics, during the academic year 2023-2024.

Prof. Surjeet Singh

Committee:

Prof. Surjeet Singh

Prof. Prasenjit Ghosh

This thesis is dedicated to our Lab 210

Declaration

I hereby declare that the matter embodied in the report entitled "Study of Thermoelectric Behavior of some Double and Triple half-Heuslers" are the results of the work carried out by me at the Department of Physics, Indian Institute of Science Education and Research, Pune, under the supervision of Prof. Surjeet Singh and the same has not been submitted elsewhere for any other degree. Wherever others contribute, every effort is made to indicate this clearly, with due reference to the literature and acknowledgement of collaborative research and discussions.

S.S.Vishak (Roll no.: 20191093)

Acknowledgments

Firstly, I would like to express my gratefulness to my supervisor Prof. Surjeet Singh. The enormous counsel and support provided by him at the initial stages of my research career, as I entered the field wide-eyed with passion, were directly responsible for my scientific vocation to realize into a credible approach, a *solid state*. I'm truly inspired by him and would always look up to him as a guiding light for how to approach research. I would also like to thank my expert Prof. Prasenjit Ghosh for his valuable guidance and critical remarks throughout that have very much helped in shaping up my work.

I'm very much thankful to my PhD mentor Ankit for almost literally guiding me by hand throughout the laboratory life. From teaching me the techniques to explaining the conceptual frameworks with zeal, he has taught me a lot with regards to research, and has been accepting of my ideas and insights with an open mind. Also, his life insights are valuable and definitely entertaining. I'm also thankful for his tolerating my spontaneous launches of insights and information. I'm extremely grateful to my dear labmates: Luminita ma'am, Dinesh, Navita, Lalith, Sagar, Dibyata, Nashra, Pankaj, Rupesh, Appu, Prabhu, Arindam, Anuja, Divya, Vijayalaxmi, and Abhishek, for them wholly accepting me as part of the tribe and so harmoniously enriching my lab life.

I would like to thank IISER Pune for providing this nonpareil environment for me to embark on my work. I sincerely thank Nilesh, Sudhir, Karthikeyan, and the entire staff of h-cross and the administrative staff for their support. I'm also thankful to INSPIRE and KVPY for the fellowship.

I gratefully appreciate the ensemble groups of friends that I have amassed at IISER Pune. I'm very much thankful for their continuous upliftment of my spirits and all the fun throughout the months.

I'm very much grateful to my teachers, for without whose lessons and understanding, I would not be the person I am.

Lastly, I am indebted to my family for everything. Their unwavering faith in me even when I wavered is the reason I am who I am. Also, I would like to thank God. For life is our reaction to encounters, but the encounters are predominantly chance encounters. Therefore, it is upto that chance, that I have ended up here, now, as whatever I am. And I'm pretty grateful for how it has turned out.

"He who has a why, can bear almost any how." — Friedrich Nietzsche

Abstract

Thermoelectricity is a promising technique to tackle the worldwide energy demand, pollution and resource depletion, which harvests energy by the direct conversion of waste heat into electricity. The limiting factor of this approach to practical power generation remains the low efficiency of the interconversion, which is evaluated in terms of a dimensionless figure-of-merit $zT = S^2\sigma T/(\kappa_L + \kappa_e)$, where S is the Seebeck coefficient, σ is the electrical conductivity, κ_L is the lattice part of thermal conductivity, κ_e is the electronic part of thermal conductivity, and T is the absolute temperature.

The half-Heusler systems are a promising class for mid-to-high temperature range thermoelectric utilization. These are ternary compounds of composition XYZ where X and Y are transition metals and Z is a p-block element. They show high thermal and mechanical stabilities and semiconductor-like transport properties. The aim remains to decrease their inherently high lattice thermal conductivity and improve their electronic transport properties further using various methods of enhancement, thereby improving the material's zT.

The aim of this project was to synthesize and characterize some new double and triple half-Heusler alloys (DHH and THH) of the form $XY_{0.5}Y'_{0.5}Z$ and $XY_{0.33}Y'_{0.33}Y''_{0.33}Z$, respectively. The synthesis was done by the method of arc melting and then consolidating the ground sample into a high-density pellet utilizing a hot-press. The structural and thermoelectric characterization (electronic transport and thermal properties) were carried out on the synthesized samples. Minimization of lattice thermal conductivity was carried out to reach a minimum of 1.8 $Wm^{-1}K^{-1}$ for the THH. Further tuning of the Fe-Ni ratio was performed to obtain n-type and p-type counterparts. The n-type ($zT = 0.40$) was found to be superior to the p-type ($zT = 0.14$) in its thermoelectric properties, and therefore p-type was further improved via a decrease in Co concentration to reach a peak zT of 0.32.

Contents

List of Figures

List of Tables

Chapter 1

Introduction

The observation of the annual energy production and usage provides two alarming conclusions: the dependence on fossil fuels as the primary source of energy and the fraction of the total available energy that is effectively put to use. From Figure 1.0.1, one can infer that about 70% of the energy obtained from all energy sources, renewable and non-renewable, is being wasted as rejected heat [1]. Therefore, it is of utmost importance to effectively harness this enormous reserve of energy. For these reasons, thermoelectric materials have garnered increased attention, due to their ability to convert heat into electricity and vice-versa directly, i.e. without intermediate processes. This has led to the search for effective thermoelectric materials, for they have huge potential in primary energy generation as well as waste energy harvesting. The advantages these thermoelectric modules have are that they do not produce harmful gaseous exhaust, are noiseless, and require low maintenance (no moving parts). But they also have the challenges of the need to raise their efficiency and lowering the fabrication cost, which thereby form the predominant concerns of the thermoelectric community [2].

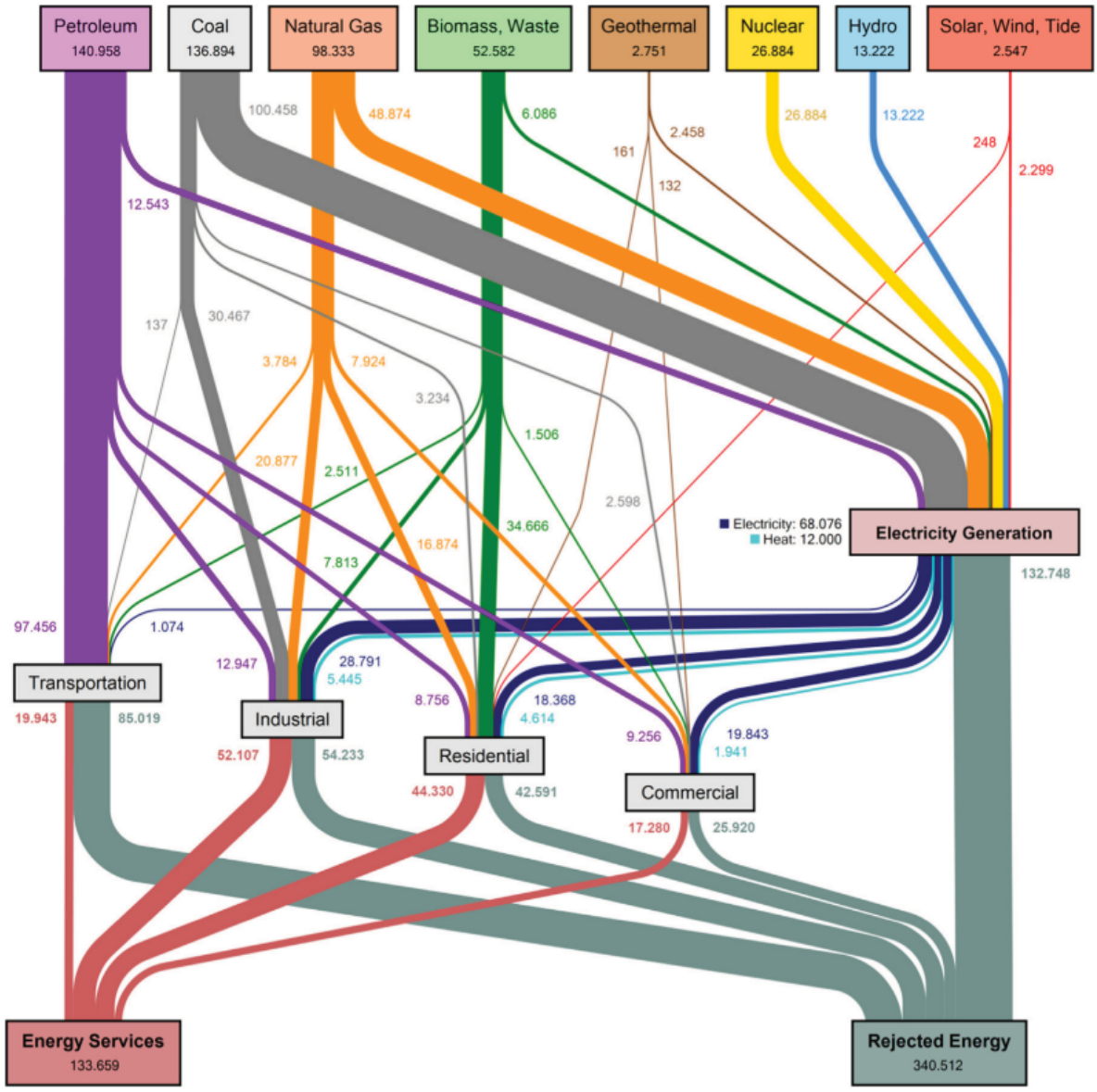

Figure 1.0.1: Energy production and consumption of the world in 2012 in PJ (adapted from [1])

Thermoelectric generators utilise the Seebeck effect (as discussed in the following sections) to generate electricity from a temperature gradient. As depicted in Figure 1.1.1, the two legs (p-type and n-type) are connected electrically in series and thermally in parallel to construct the device. It is preferred to have both legs of similar materials for the device fabrication,

as the reactivity of the thermoelectric material with the metal electrodes at the hot end of the device has been a serious issue for the longevity of the device. The maximum efficiency of a thermoelectric device is given by [3]:

$$\eta_{max} = \frac{T_h - T_c}{T_h} \frac{\sqrt{1 + Z\bar{T}} - 1}{\sqrt{1 + Z\bar{T}} + \frac{T_c}{T_h}}$$

where T_c, T_h, and $\bar{T}$ are the cool side temperature, hot side temperature, and the average temperature across the device, respectively. The dimensionless quantity $Z\bar{T}$ is the average thermoelectric figure of merit of the device, and the thermoelectric figure of merit of the individual legs is denoted by zT, which is defined as $zT = \frac{S^2 \sigma T}{\kappa}$, where S is the Seebeck coefficient, σ is the electrical conductivity, T is the absolute temperature, and κ is the thermal conductivity of the material [2].

1.1 Thermoelectricity

Thermoelectricity is the direct interconversion of energy i.e. between heat and electricity. In this phenomenon, a temperature gradient across the material or device would drive the current by generating a potential difference or a potential difference is utilized to create a temperature difference. The bracket of thermoelectric effects comprises three constituent effects - the Seebeck effect, the Peltier effect, and the Thomson effect.

1.1.1 Seebeck Effect

The Seebeck effect was initially observed by Alessandro Volta in 1794. The thermoelectric effect named after Thomas Johann Seebeck, was mischaracterized by the same as the "thermomagnetic effect" when he rediscovered it in 1821 (where he joined two dissimilar metals in a closed loop and maintained the two joined ends at different temperatures and found that this loop deflected a magnetic compass). It was only later the term "thermoelectricity" was coined by Hans Christian Oersted, who correctly stated that a current was driven due to the temperature gradient that then in turn gave rise to a magnetic field.

Therefore, the Seebeck effect can be described as the generation of potential in a material when a temperature gradient is set up across the same. The potential built up when a steady state is achieved in the material is mathematically expressed as $\Delta V = -S\Delta T$ where ΔV is the voltage built up, ΔT is the temperature difference, and S is the material's Seebeck coefficient (also known as the thermopower).

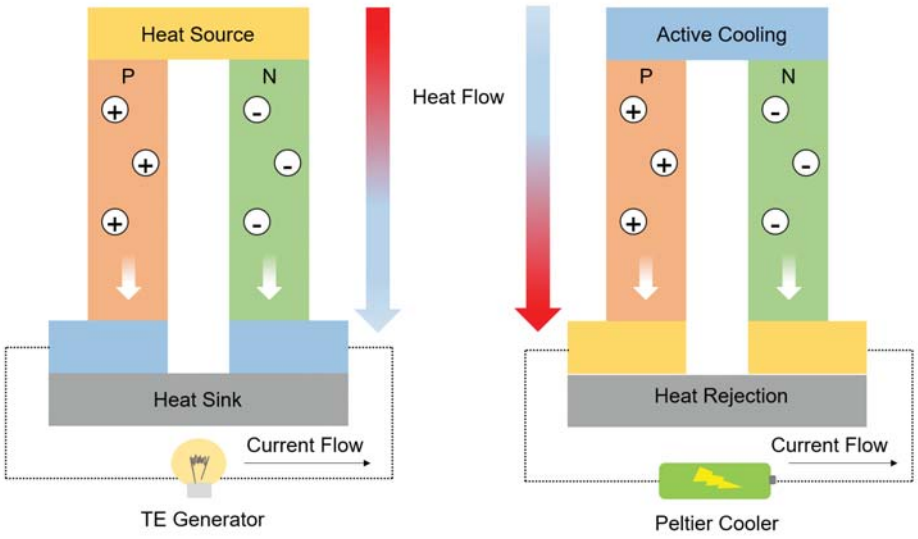

Figure 1.1.1: Schematics of Seebeck effect and Peltier effect

1.1.2 Peltier Effect

In 1834, Jean Charles Athanase Peltier, discovered this effect, thereby it getting named after him. He observed the reversed scenario of the Seebeck effect, that is, when an electric current is passed through a material, a temperature gradient is created across it. This can be denoted as $\dot{Q} = \Pi I$, where $\dot{Q}$ is the heat generation rate at a junction, Π is the Peltier coefficient of the material, and I is the current. This Peltier coefficient is related to the aforementioned Seebeck coefficient by $\Pi = ST$. This Peltier effect is utilized in thermoelectric cooling systems.

1.1.3 Thomson Effect

This effect is named after Lord Kelvin (born William Thomson), who predicted and then verified the effect in 1851. This effect explains the continuous absorption and evolution of heat across the material with a temperature difference across it and an electric current passing in it. The rate of heat generation is expressed as $\dot{Q} = -\tau \vec{J} \cdot \vec{\nabla} T$, where $\vec{J}$ is the current density, and τ is the Thomson coefficient.

In 1854, Kelvin related the three coefficients (Seebeck, Peltier, and Thomson) to give two relations. The first Thomson relation is $\tau = \frac{d\Pi}{dT} - S$ and the second Thomson relation is $\Pi = ST$. Now, using the second relation, the first Thomson relation becomes $\tau = T\frac{dS}{dT}$.

1.2 Thermoelectric Devices

Thermoelectric devices for practical applications are usually composed of multiple modules that are connected serially in terms of electrical and parallelly in terms of thermal passage, wherein each module consists of a p-type and an n-type leg. Consider its usage for thermoelectric cooling. The quantity that is defined as the proportion of the heat absorbed from the source to the amount of electrical energy spent is termed the coefficient of performance (COP). In the absence of resistive losses and losses in heat conduction, COP would reach the ideal value, the Carnot cycle's value.

The ideal COP is given by $T_h/(T_h - T_c)$ where T_h is the absolute temperature of the source and T_c is that of the sink. The most effective coefficient of performance of a thermoelectric cooler ϕ_{max} is given by $\phi_{max} = \frac{T_h[(1+Z\bar{T})^{1/2} - (Tc/Th)]}{\Delta T[(1+Z\bar{T})^{1/2}+1]}$, where device figure of merit Z is given by $Z = \frac{(S_p - S_n)^2}{[(\kappa_p \rho_p)^{1/2} + (\kappa_n \rho_n)^{1/2}]^2}$. Here S_p and S_n refer to the S of the p-type and n-type legs respectively. Similarly, the respective thermal conductivities and resistivities are represented by κ and ρ. [4]

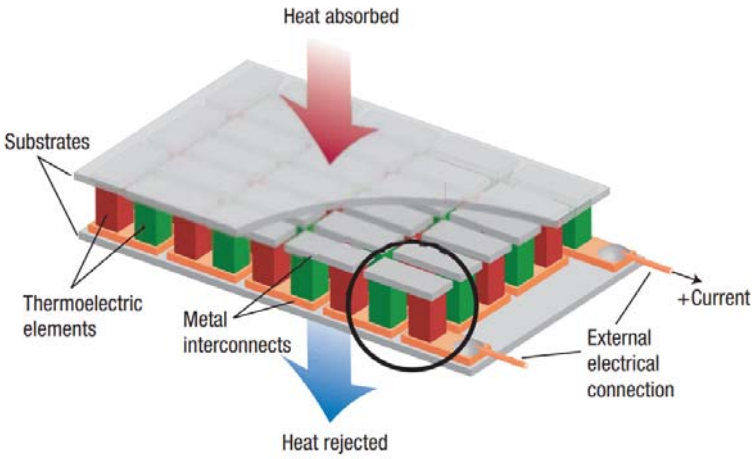

Figure 1.2.1: Thermoelectric device (adapted from [5])

In the case of thermoelectric generators, the efficiency is similarly given by η:

$$\eta = \frac{\Delta T[(1 + Z\bar{T})^{1/2} - 1]}{T_h[(1 + Z\bar{T})^{1/2} + (T_c/T_h)]}$$

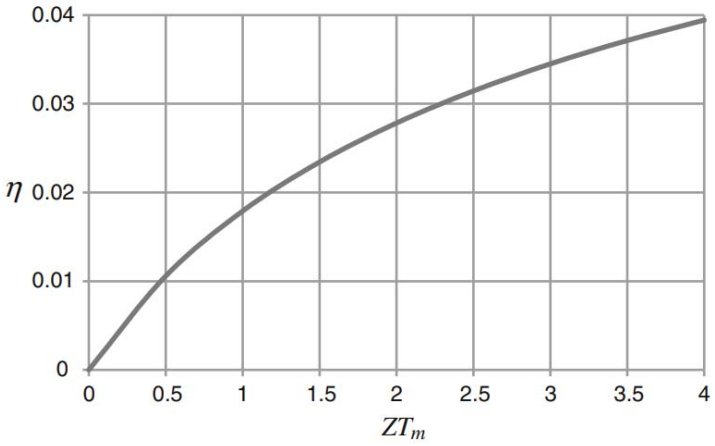

Figure 1.2.2: Efficiency vs ZT (adapted from [4], with $T_h = 400$K and $T_c = 360$K)

From the aforementioned relation (and Figure 1.2.2), one can see how the efficiency is dependent on the figure-of-merit and hence see the merit in raising the zT.

1.3 Transport Coefficients

As mentioned earlier, the material figure-of-merit is designated as $zT = \frac{S^2\sigma T}{\kappa}$. As can be seen, the zT depends on certain physical properties of the material (the charge and thermal transport) and therefore the understanding of the same is required for the selection and enhancement of materials for better zT.

Seebeck Coefficient

The Seebeck coefficient is described as $S = -\Delta V/\Delta T$, where ΔV is the potential built up due to the temperature gradient ΔT across the material. Now, in the single parabolic band (SPB) model:

$$S = \frac{8\pi^2 k_b^2 m^* T}{3eh^2}(\frac{\pi}{n})^{2/3}$$

where k_b is the Boltzmann constant, h is the Planck's constant, e is charge, n is the carrier concentration, and m^* is the density of state (DOS) effective mass. The DOS effective mass is related to band valley degeneracy N_V and band effective mass m_b^* as $m^* = N_V^{2/3} m_b^*$ [6].

Electrical Conductivity

The electrical conductivity of a material is specified as σ and can be expounded as $\sigma = ne\mu$, where μ is the mobility. In the case of a system with two types of carriers, it can be expressed as $\sigma = n_h p\mu_h + n_e e\mu_e$.

The power factor is specified as $PF = S^2\sigma$. As we can see from the two aforementioned quantities, we can see how they're interrelated [4].

Thermal Conductivity

The thermal conductivity κ comprises :

$$\kappa = \kappa_L + \kappa_e$$

where κ_L is the lattice part of thermal conductivity and κ_e is the electronic part of thermal conductivity. The electronic part is related to the electrical conductivity by

$$\kappa_e = \sigma LT$$

where L is the Lorenz number. The Lorenz number for doped semiconductors can in turn be obtained from the Seebeck coefficient as $L = 1.5 + exp(\frac{-|S|}{116})$ [7].

The lattice thermal conductivity, κ_L, can be defined by $\kappa_L = \frac{1}{3} C_V v l$, where C_V is the lattice heat capacity per unit volume, v is the sound velocity, and l is the mean free path of phonons ($l = v\tau$, τ is the relaxation time) [4].

As we can see from these relations and Figure 1.3.1, except κ_L, other quantities (S, σ, and κ_e) are interrelated and hence achieving a higher zT would mean to hit the sweet spot where the combination of these quantities yield a maximum.

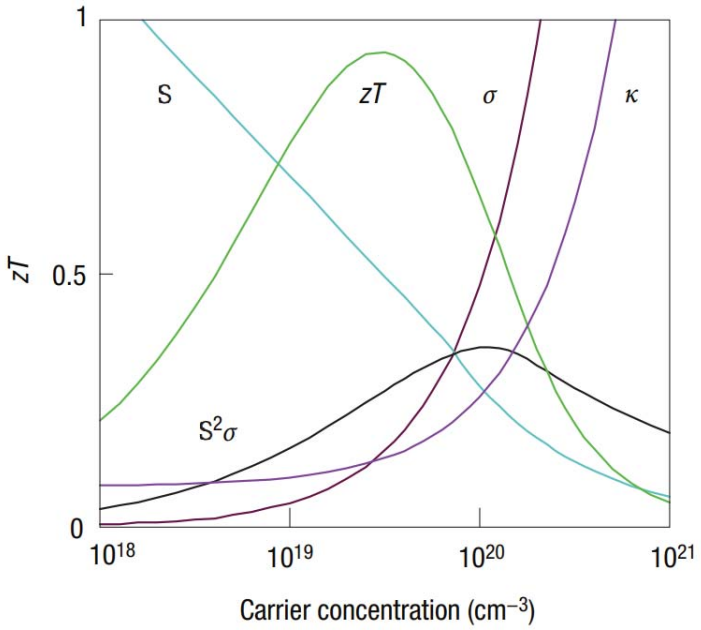

Figure 1.3.1: The plot to show the interrelations of the various physical quantities (adapted from [5])

1.4 Strategies for improving the zT

With regards to the aim of the betterment of the thermoelectric figure of merit, zT, two major approaches have been undertaken, which can be deduced from the previous sections - increasing the PF and decreasing the κ_L. A few of the pathways that have been employed to achieve the same are explored in this section.

1.4.1 Enhancing the power factor

Carrier Optimization

As seen from the plot in the previous section (Figure 1.3.1), the peak PF is achieved at an optimum carrier concentration, due to the S varying inversely with n and σ linked proportionately with n. This leads to the employing of optimizing the n as the strategy of increasing the PF, thereby increasing the zT, and has been carried out in multiple cases successfully [8].

Modulation Doping

Modulation doping differs from ordinary doping as the charge carriers are physically separated from the ionized dopants, i.e. the dopant phase is separate from the bulk matrix through which conduction occurs. The carriers flow from the dopant-phase grains onto the bulk, whereas the ionized dopants are in the grains. This results in a reduction of the carrier scattering by ionized impurities, thereby enhancing the mobility [10]. This method is schematically portrayed in Figure 1.4.1.

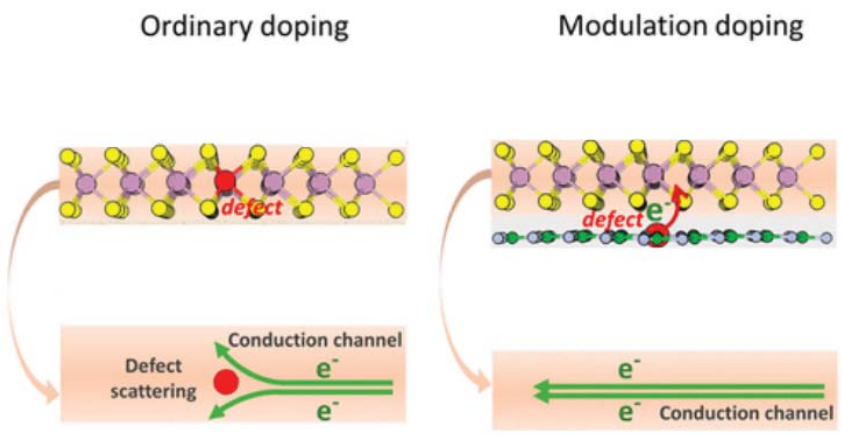

Figure 1.4.1: A schematic for modulation doping (adapted from [9])

Resonant Doping

In the case of resonant doping, a small amount of doping results in a conspicuous increase in the power factor, PF. This happens because of the doping induced distortion in the density of states near the Fermi level, causing an increase in the band effective mass, thereby increasing the S. This in turn enhances the PF [11].

Band Convergence

This occurs when bands come into alignment, such as by virtue of a dopant. It leads to an increase in band degeneracy N_V and raises the density of states effective mass m^*, which in turn enhances the Seebeck coefficient S, thereby increasing the figure of merit zT [12].

Energy Filtering

Energy filtering effect, as the name suggests, employs the obstructing effect of energy barriers on carriers of lower energy while only allowing those of higher energy to freely flow. This results in the decoupled nature of the two quantities in electrical conductivity: a decrease in charge carriers in conduction but an increase in mobility. This leads to σ not being affected largely while enabling the enhancement of S [13].

1.4.2 Decreasing the thermal conductivity

Alloying or Doping

Doping a site with a small amount of another element would lead to point defect scattering of phonons. Alloying similar compounds, which is effectively the substitution of a site by atoms that are often the same group (thereby retaining valence electron count and chemical nature) but of different mass, leads to a considerable diminution in lattice thermal conductivity κ_L by virtue of mass fluctuation [3, 14].

Nanostructuring

The inclusion of nanoparticles and formation of nanograins result in the scattering of phonons of higher mean free paths (l). This results in a wider range of phonons being scattered, thereby resulting in decreased lattice thermal conductivity [15].

1.5 Thermoelectric Materials

Various thermoelectric materials have been extensively explored during the last few decades. **Chalcogenides**, with their low thermal conductivities, have shown exceptional performances in the low to medium temperature range. Examples include PbTe, GeTE, and Bi_2Te_3. **Clathrates, Oxide materials, Skutterudites, Zintl phase compounds, Mg-based materials**, etc. are a few of the other investigated classes of thermoelectric materials [2].

The class of materials in this study is that of **half-Heuslers** (hH). Named after Friedrich Heusler, these ternary intermetallic compounds have the chemical formula of the form XYZ, where X and Y are transition metals and Z is a p-block element. They crystallise in the space group $F\bar{4}3m$ (no. 216), which comprises three interpenetrating FCC sublattices. X is the most electropositive element and occupies the 4a site, Y occupies the 4c site and has the intermediate electronegativity, and Z is the most electronegative element and occupies the 4b site. In Figure 1.5.1, X is depicted in red, Y in blue, and Z in green. They predominantly

stabilise with a valence electron count, VEC, of 18[2]. Their semiconducting nature is evident from Figure 1.5.2.

Half-Heuslers offer various beneficial factors such as high thermal stability, excellent mechanical strength, potential for tunability of sites, reasonable cost, generally non-toxic composition, and exceptional thermoelectric properties in the mid-to-high temperature range, owing to their relatively high power factors [17].

The primary challenge in these systems is the intrinsically high lattice thermal conductivities (κ_L). Various methods have been employed and are being explored towards reducing their κ_L, thereby raising their zT. In this regard, the so-called **double half-Heuslers** have proven to be promising[17]. These are in reality alloys, with two atoms occupying a site, yet the terminology is prevalent. They are often denoted in literature in their expanded chemical formula $X_2YY'Z_2$, but owing to their real nature as alloys or solid solutions, the actual chemical formula $XY_{0.5}Y'_{0.5}Z$ is the more appropriate representation. By the aliovalent substitution at one site, with the aim to maintain the valence-balanced composition, the double half-Heulsers are obtained. For example, $TiFe_{0.5}Ni_{0.5}Sb$ is a double half-Heusler with the Fe and Ni substitution at the Y-site, where TiFeSb has a VEC of 17 and that of TiNiSb is 19. This has led to a marked minimization in the κ_L in comparison to respective parent compounds (the room temperature κ_L drops from ~ 20 $Wm^{-1}K^{-1}$ for TiCoSb to $7-9$ $Wm^{-1}K^{-1}$ in the case of $TiFe_{0.5}Ni_{0.5}Sb$[17, 18]. The further advantage of such systems has been that they offer in-site tuning options by just shifting the ratios of the Y-site components away from the equimolar case, thereby generating p-type and n-type counterparts.

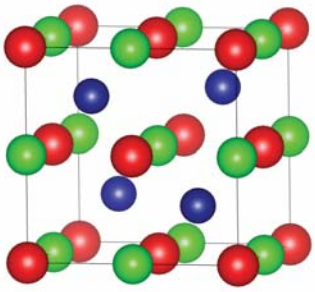

Figure 1.5.1: A representation of the structure of a half-Heusler

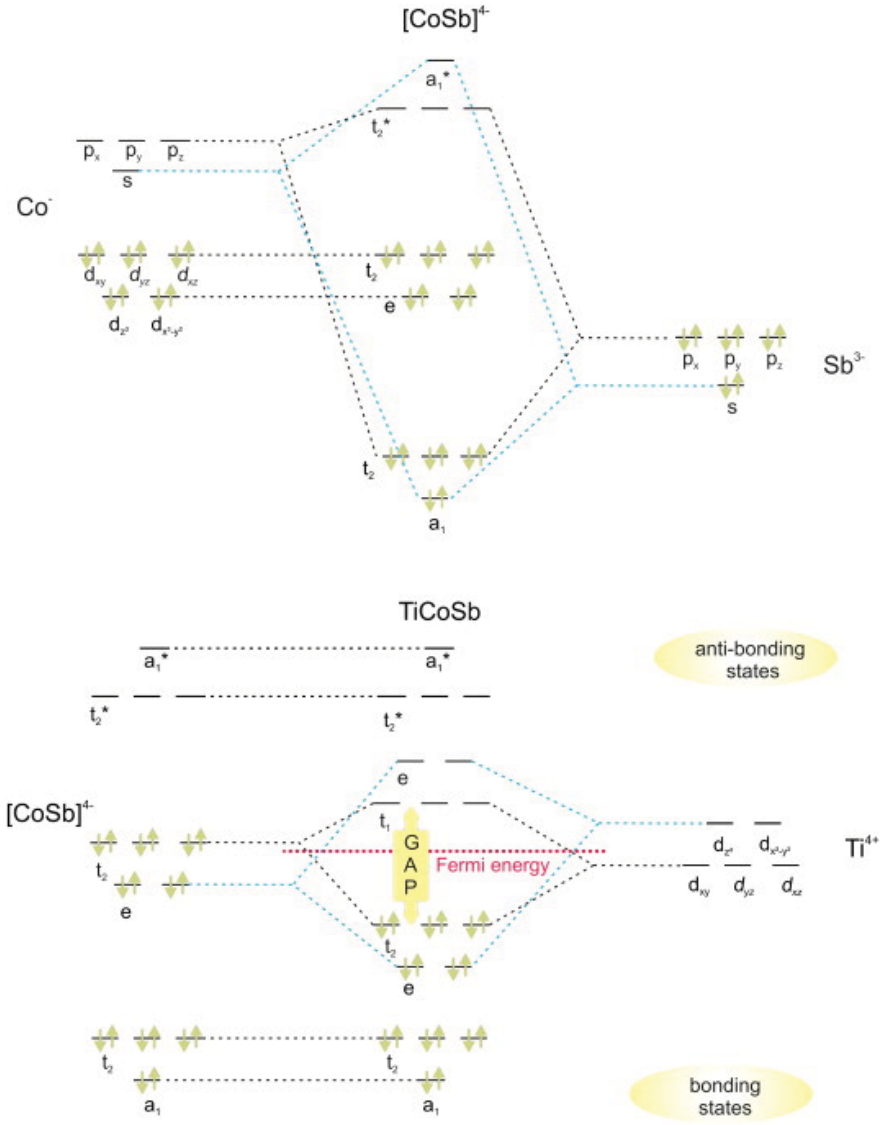

Figure 1.5.2: Molecular orbital picture of 18 VEC TiCoSb (adapted from [16])

Motivated by this idea, various possibilities to bring down the κ_L of half-Heusler systems have been explored. Double and triple half-Heusler alloys, by aliovalent substitution and also alloying of isovalent compositions, were synthesized to augment the thermoelectric properties and also obtaining n-type and p-type materials with the same starting elements.

Chapter 2

Experimental Techniques

2.1 Synthesis

Primary synthesis of the sample was carried out by arc-melting in a high-purity argon atmosphere. The ingots were then hand-ground and consolidated in the Vacuum Hot-Press, thereby effectively resulting in dense pellets.

2.1.1 Arc Melting

The initial procedure in preparing the samples was to prepare ingots by the method of arc melting. The arc melting system consists of an inert chamber, a vacuum system, and a power source connected to the Tungsten electrode. Proportional amounts of the precursors (high purity, elemental) by weight are loaded onto the concave grooves in the copper hearth (which is continually cooled by the water circulation from the chiller). The chamber is then vacuumed (using a rotary pump, reaching a minimum pressure of about 3×10^{-2} mbar) and filled with Argon, a sequence of purging and filling, five times to ensure maximal evacuation of atmospheric gases from the chamber to avoid oxidation of the melt. The electric arc is generated from the tungsten tip (whose movement is controlled from outside). A piece of Zirconium is used as a getter; initially melted every time before the melting of the sample to ensure residual oxygen is also removed. The precursors are then melted and the resultant

ingot is flipped and remelted thrice for homogenization.

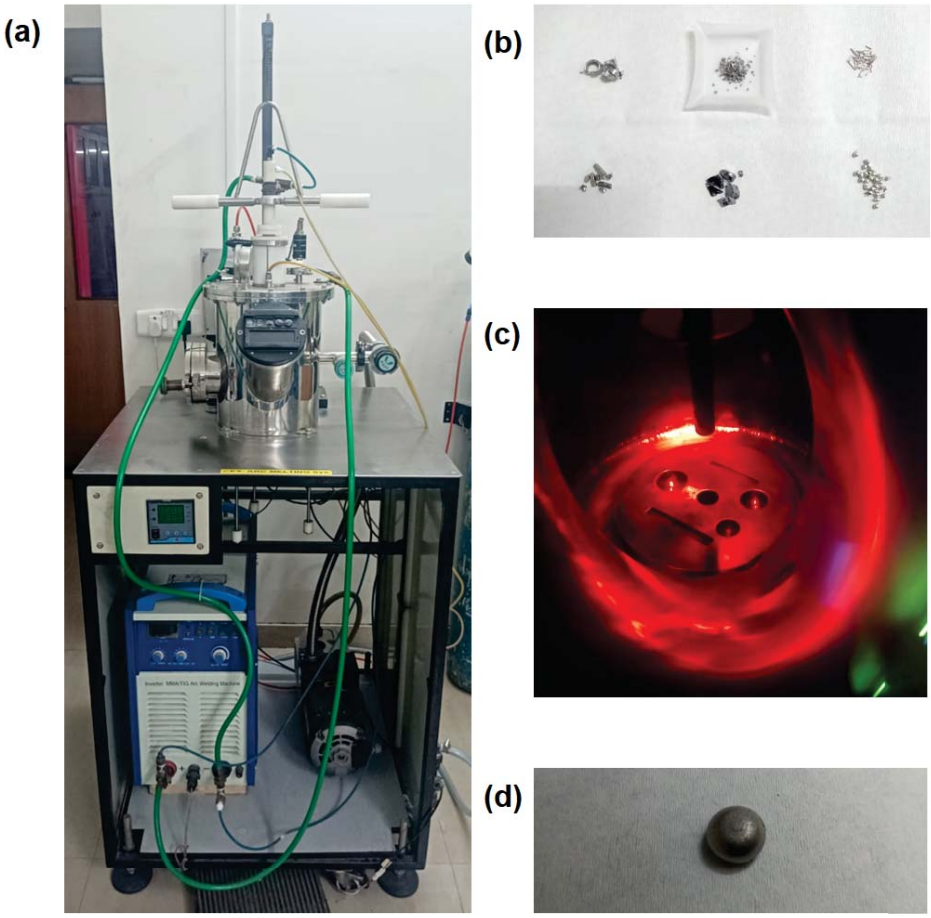

Figure 2.1.1: (a) Arc melting system, (b) Elements taken for arc melting, (c) Interior of the arc melting chamber, and (d) Arc melted ingot

A point to be taken into consideration during the preparation of the samples was that antimony (Sb) has a pretty low boiling point (1587 °C). Therefore, the synthesis protocol was optimized by taking an additional 10% of Sb to compensate for the losses during the melt and to avoid non-stoichiometry of the samples. Also, due to the antimony vapours obstructing the viewing quartz windows and quartz window of the light source, purging the vapours and filling argon is performed for every melt.

2.1.2 Hot Press

Vacuum Hot-Press (VLT-VHP) is utilized to consolidate the samples into dense pellets. The ingots were, via an agate mortar-pestle set, hand-ground for one hour. This powdered sample was loaded onto graphite die-sets of internal diameter of about 10.3 mm, whose internal surface area is covered with thin graphite sheets to prevent the sample from sticking to the surface of the die-set. These die-sets are loaded into the Hot-pressing chamber, which is then evacuated (to about 2×10^{-2} mbar) and maintained in a dynamic vacuum throughout the process. An induction coil encloses the die set and is used for heating, while a pyrometer placed outside detects the temperature of the die set through a quartz window. The temperature protocol was optimized following multiple trials of consolidation of similar samples. The samples were initially taken to and maintained at 750^oC for five minutes and then taken to and densified at 1070^oC for five minutes under a pressure of 56 MPa.

Figure 2.1.2: Vacuum Hotpress machine

2.2 Characterization

The prepared samples are cut using a low-speed diamond saw in shapes as shown in Figure 2.2.1. A bar-shaped piece is cut and prepared for the electrical resistivity (ρ) and S measurement while the major segment of the disc is used for the thermal conductivity (via diffusivity) measurement. The remainder minor segment is broken and ground for PXRD. All pieces prepared are polished thoroughly prior to the measurements.

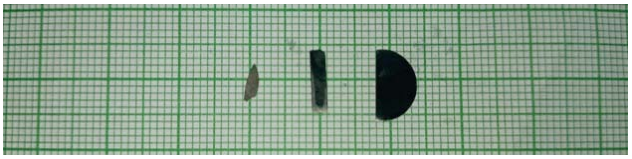

Figure 2.2.1: Cut pieces of the sample for measurements

2.2.1 Powder X-Ray Diffraction (PXRD)

The structural characterization (Powder XRD) was carried out in a Bruker D8 Advance Diffractometer. X-ray diffraction is the primary crystallographic tool for the structural characterization of crystalline materials. It employs Bragg's law to procure information on the structure of the material. When electromagnetic radiation of the X-ray regime falls on the materials, the lattice planes behave as a diffraction grating for the same. Peaks are obtained following constructive interference, and they follow Bragg's rule :

$$n\lambda = 2dsin\theta$$

where λ is the wavelength of the incident radiation, d is the interplanar spacing, and θ is the angle between the incident x-ray and the lattice plane. The source and detector rotate, thereby collecting data over a range of 2θ.

The sample was ground into fine powder, and with the help of oil, stuck onto glass slides and loaded onto the diffractometer's sample holder. The source of radiation is Cu target, therefore the wavelength of $K_{\alpha 1}$ is 1.54060 $\mathring{A}$ ($K_{\alpha 2}$ was stripped, along with the background, using the EVA software, for plotting). The purity of the sample was verified and impurities

were identified using the XRD database of the EVA software. The XRD plots were plotted using Origin graphing software as peak intensity vs the 2θ in degrees. Rietveld refinement was performed using FullProf software.

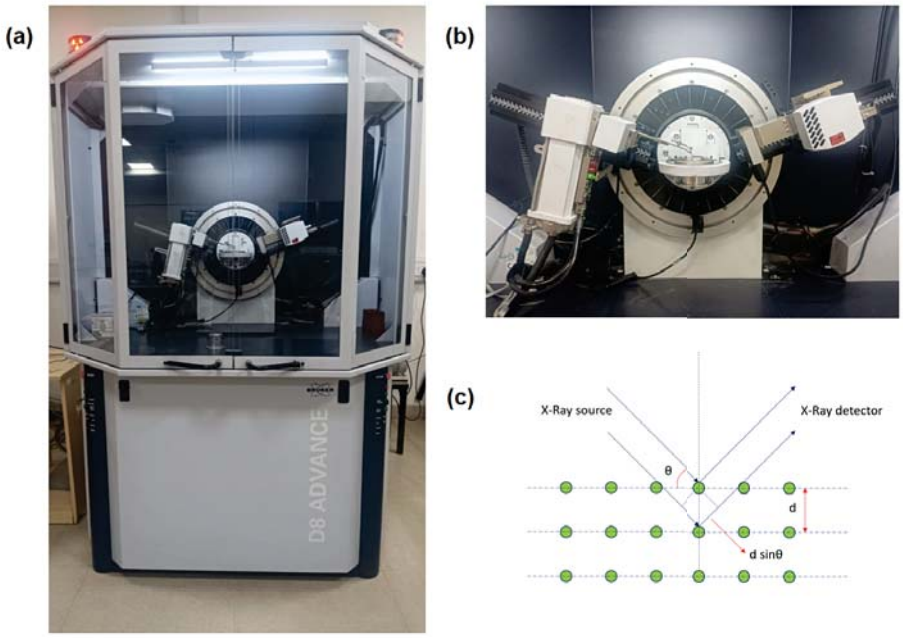

Figure 2.2.2: (a) X-ray diffractometer, (b) The interior of the diffractometer, (c) A schematic to explain X-ray diffraction

2.2.2 Seebeck and Resistivity measurement (LSR)

Electrical resistivity (ρ) and Seebeck coefficient (S) measurements were performed using the LSR-3 (Linseis) setup. The setup measures the ρ and S simultaneously from room temperature to a thousand degrees Celsius for solid materials. The measurements are done in an inert chamber, that is purged and filled with He gas (four cycles). As mentioned before, the measurements were performed on bar-shaped pieces of the samples (cuboidal). The contacts are all pressure contacts. A current between ten and a hundred milliamperes can be utilized, and a ΔT of up to 50 K could be established between the upper and lower electrodes. Heating of the chamber is achieved via halogen lamps at its corners, and a

nickel jacket is used to get a uniform heating environment enclosing the sample. The outer compartments are cooled via water circulation. Samples were measured with a constant current of 20 mA across the two electrodes.

Figure 2.2.3: LSR-3 setup for Seebeck and resistivity measurements

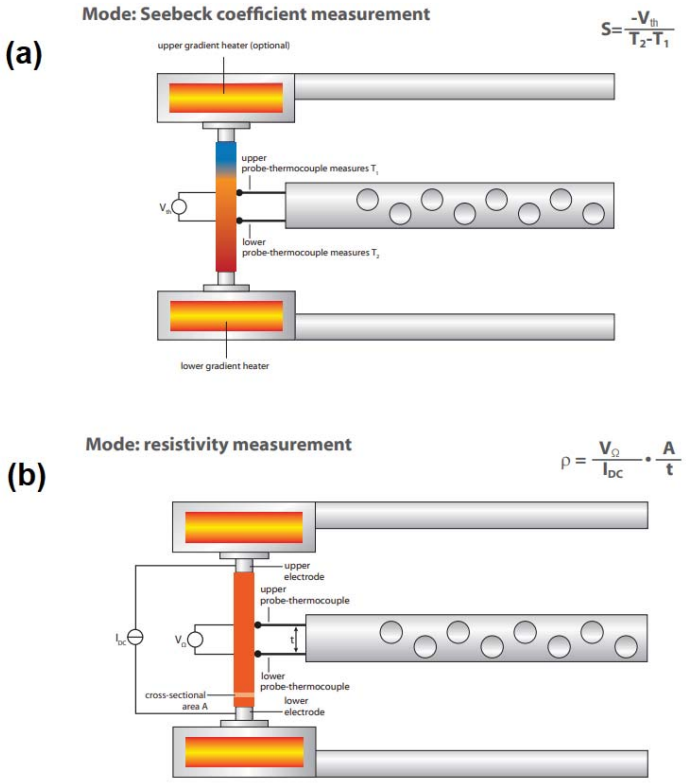

Figure 2.2.4: Schematics showing (a) Seebeck coefficient measurement and (b) Electrical resistivity measurement (adapted form Linseis LSR-3 manual)

The ΔV is measured across the two centrally placed s-type thermocouples. Using $\rho = \frac{\Delta V A}{It}$, ρ (resistivity) is measured (A is the cross-sectional are and t is the interprobe distance). Seebeck coefficient is measured by virtue of the heater in the lower electrode that maintains a ΔT of 40 K across the sample, thereby getting the relative Seebeck coefficient via $S = -\Delta V/\Delta T$. Using the Ta.exe software that contains the standard data of the instrument system contribution, the sample's absolute Seebeck coefficient S is obtained.

2.2.3 Laser Flash Analyzer (LFA)

The thermal diffusivity (D) of the sample is procured from LFA-1000 (Linseis). From the thus obtained D, κ is extracted using the formula $\kappa = D\rho C_P$, where ρ is the density of the material and C_P is the specific heat, which was taken as the value corresponding to the Dulong-Petit limit ($3nR$). The samples were taken in thin major-segment-shaped pieces, coated with graphite spray for effective heat absorption. The chamber is evacuated and filled with He gas (three to four cycles) and the measurement is carried out under a dynamic vacuum. Liquid nitrogen is used to cool the infrared detector, by regular filling of its Dewar.

Figure 2.2.5: LFA-1000 setup for thermal diffusivity measurements

The temperature is increased and maintained (measured till 800 °C) and a laser pulse is emitted. The diffusion of the heat across the sample piece is detected by the IR detector, from which the time taken for diffusion is used in the relation that follows to calculate the diffusivity : $D = \frac{0.13879\, l^2}{t_{1/2}}$, where l is the sample thickness and $t_{1/2}$ is half of the time that was taken for it to achieve the maximum temperature. Heating (from room temperature till 800 ^{o}C) and cooling sections (back to room temperature) comprise each run. Three measurements are taken at each temperature during the section of the run and a fitting of above 96% is programmed to be routinely checked for before the accepting of the data point by the software. The chamber of measurement and the laser systems are cooled by water circulation.

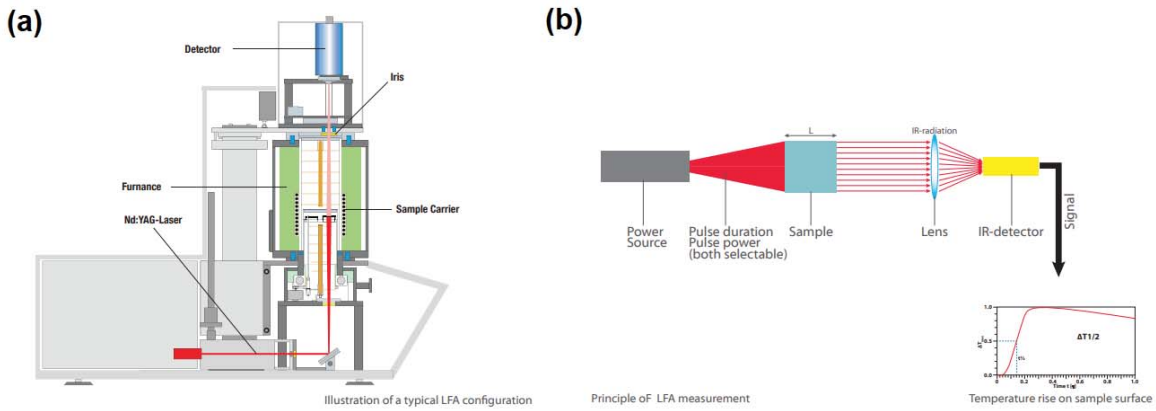

Figure 2.2.6: Schematics for (a) LFA setup and (b) Thermal diffusivity measurement (adapted from the LFA manual)

Chapter 3

Results and Discussion

The work carried out in this thesis is split into five phases. In the first phase, the minimization of lattice thermal conductivity was focused on by the idea of synthesizing complex half-Heuslers - Double and Triple half-Heuslers. The second phase focuses on synthesizing the p-type and n-type compounds from the same starting triple half-Heusler alloy. The following phases focus on the betterment of the p-type, starting with the subsequent reduction of the Cobalt fraction in the material.

3.1 Phase - I : Reduction of Lattice Thermal Conductivity

The class of materials under our consideration in the study is that of half-Heuslers. Half-Heuslers, as we have seen earlier, are desirable candidates for thermoelectric applications. ZrNiSn-based materials have been explored as high zT n-type half-Heuslers (> 1.2). In fact, the exploration of n-type half-Heuslers has been extensive [2]. The investigation into p-types has been lesser in comparison, and excluding the exceptional values of materials like ZrCoBi, TaFesb, and NbFeSb, they warrant further study.

Half-Heuslers are desirable due to their high thermopowers, great mechanical and thermal stability, comparative cost-effectiveness, and low toxicity. Their disadvantage is the inher-

ently larger values of lattice thermal conductivities. Multiple methods of minimizing of the κ_L, such as alloying and nanostructuring, have been employed to achieve the same. One such method, as discussed in the previous sections, would be the aliovalent substitution that results in double (and later triple) half-Heuslers [17].

Starting from TiCoSb and HfCoSb as the parent compounds, one can progressively move down, as shown in Figure 3.1.1. TiCoSb and HfCoSb were synthesized earlier for previous projects and have been used for the comparison of the lattice thermal conductivities. $TiFe_{0.5}Ni_{0.5}Sb$ and $HfFe_{0.5}Ni_{0.5}Sb$ were synthesized by arc-melting and hotpressing to obtain phase-pure dense pellets. The XRD patterns of the same (along with the later synthesized $Ti_{0.5}Hf_{0.5}Fe_{0.5}Ni_{0.5}Sb$ and $Ti_{0.5}Hf_{0.5}Fe_{0.33}Co_{0.33}Ni_{0.33}Sb$) are shown in Figure 3.1.2, with the *hkl* planes labelled and their lattice parameters calculated.

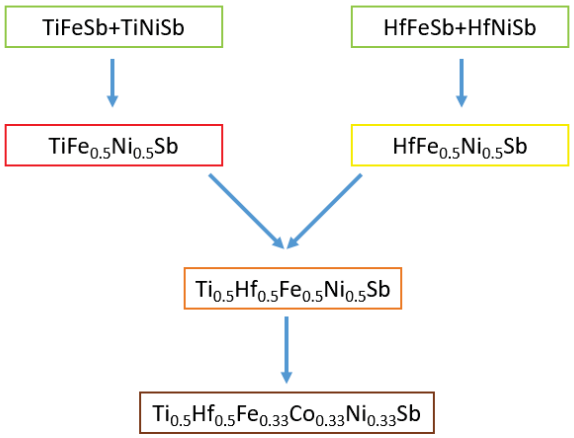

Figure 3.1.1: Flowchart depicting the idea behind the materials in Phase I

$TiFe_{0.5}Ni_{0.5}Sb$ was synthesized and verified with earlier published results. This was followed by the synthesis and characterization of the unreported $HfFe_{0.5}Ni_{0.5}Sb$, which as expected, resulted in possessing an even lower κ_L, owing to the increased mass of Hf at X site. Following this, the equimolar alloy of these two compounds, $Ti_{0.5}Hf_{0.5}Fe_{0.5}Ni_{0.5}$, was synthesized, which turned out to possess an even lower κ_L, as expected from the alloying resulting in the reduction of κ_L via mass fluctuation. This by itself had already prompted the idea of the synthesis of the triple half-Heusler (THH) alloy $Ti_{0.5}Hf_{0.5}Fe_{0.33}Co_{0.33}Ni_{0.33}Sb$.

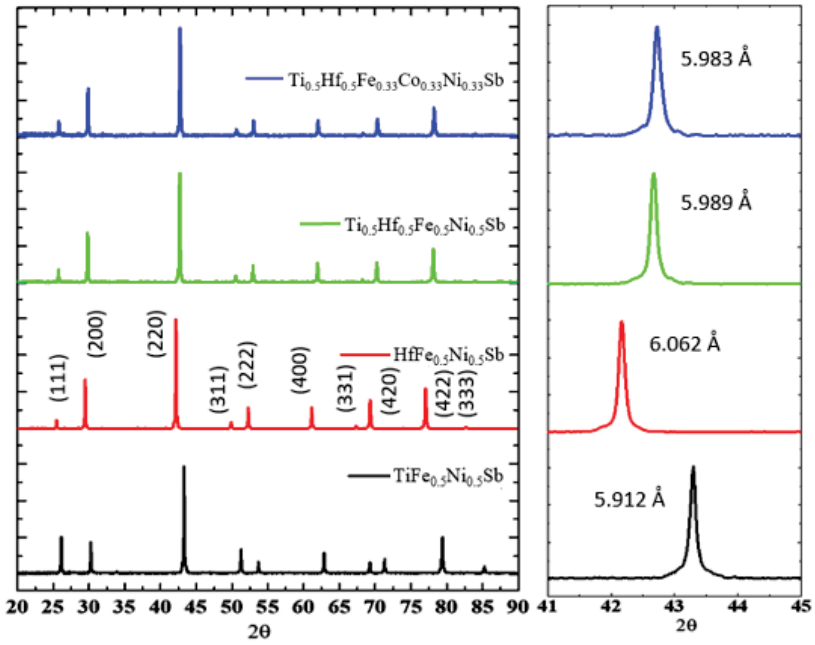

Figure 3.1.2: XRD data of materials in Phase I

The Seebeck and resistivity measurements of the double half-Heusler (DHH) alloys and THH alloy were performed using the LSR-3 setup. All of the DHH alloys were found to be p-type materials. Their Seebeck coefficient trends with temperature showed bipolarity, signalling a narrow bandgap. A bipolarity is undesirable as the high-temperature efficiency of the thermoelectric material gets compromised in such a case. The further doping of carriers by tuning the Fe-Ni ratio did help in moving the onset of bipolarity to higher temperatures, albeit slightly, but it also continued to reduce the peak Seebeck coefficient.

Further, it was calculated that the inclusion of Co in the Y-site does indeed increase the band gap and hence the compound $Ti_{0.5}Hf_{0.5}Fe_{0.33}Co_{0.33}Ni_{0.33}Sb$ was synthesized. As shown in Figure 3.1.4, the bipolarity in Seebeck did vanish from the measured range, signifying an increased bandgap. This is expected as per Vegard's law as TiCoSb has a bandgap of 1.0 eV (HfCoSb also has a similar bandgap) while $TiFe_{0.5}Ni_{0.5}Sb$ has an expected bandgap of 0.4 eV (so do the other two DHH alloys), and the resultant $Ti_{0.5}Hf_{0.5}Fe_{0.33}Co_{0.33}Ni_{0.33}Sb$ has a calculated bandgap of 0.7 eV (calculations, shown in Figure 3.1.3, were performed by Ankit Kumar). Another surprising effect of the Co introduction was the fact that this material

was intrinsically n-type. This would be of significance in the later phases and thus focused upon in the subsequent sections.

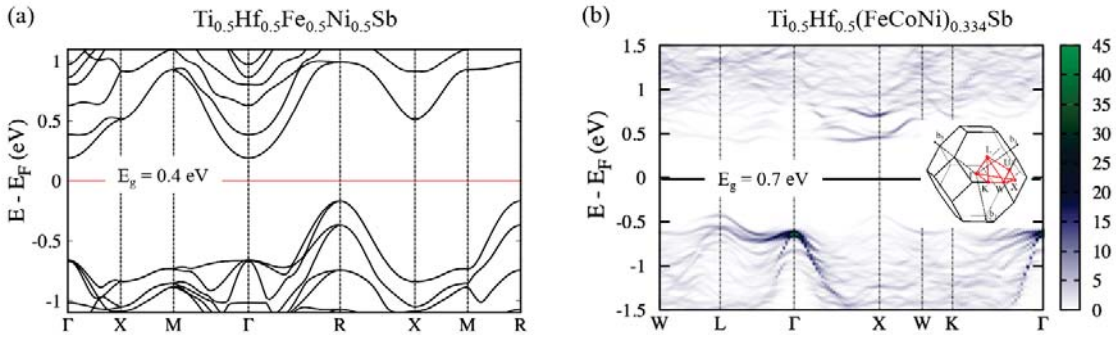

Figure 3.1.3: Band structure calculation of (a)$Ti_{0.5}Hf_{0.5}Fe_{0.5}Ni_{0.5}Sb$ and (b) $Ti_{0.5}Hf_{0.5}Fe_{0.33}Co_{0.33}Ni_{0.33}Sb$

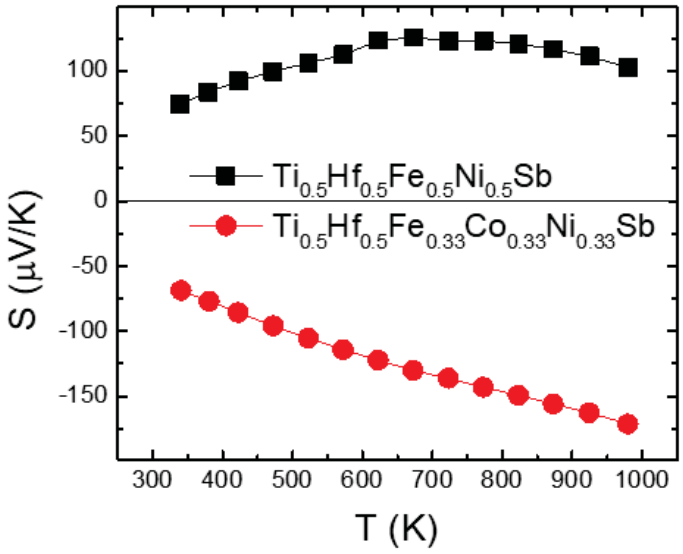

Figure 3.1.4: Seebeck data of $Ti_{0.5}Hf_{0.5}Fe_{0.5}Ni_{0.5}Sb$ and $Ti_{0.5}Hf_{0.5}Fe_{0.33}Co_{0.33}Ni_{0.33}Sb$

The thermal conductivity analysis (via the thermal diffusivity measurements) was performed via the LFA setup. The resultant plots are shown in Figure 3.1.5. Successively, the κ_L decreases, as previously mentioned, and $Ti_{0.5}Hf_{0.5}Fe_{0.33}Co_{0.33}Ni_{0.33}Sb$ showed the lowest κ_L of 1.8 $Wm^{-1}K^{-1}$.

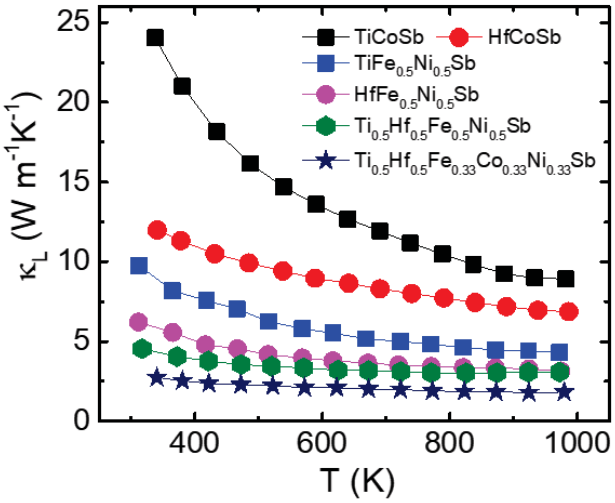

Figure 3.1.5: Lattice thermal conductivities comparison of the materials under consideration

To summarize phase I,

- A new double half-Heusler $HfFe_{0.5}Ni_{0.5}Sb$ was synthesized, which is analogous to $TiFe_{0.5}Ni_{0.5}Sb$, and was measured to have an even lower κ_L owing to the higher atomic mass of Hf.
- Synthesized $Ti_{0.5}Hf_{0.5}Fe_{0.5}Ni_{0.5}Sb$ which was found to possess a κ_L lower than either of the parent double half-Heuslers.
- Synthesized a new alloy by the inclusion of Cobalt in the Y-site i.e. $Ti_{0.5}Hf_{0.5}Fe_{0.33}Co_{0.33}Ni_{0.33}Sb$.
- This led to the observation of κ_L of these samples being of this order : $TiFe_{0.5}Ni_{0.5}Sb$> $HfFe_{0.5}Ni_{0.5}Sb$> $Ti_{0.5}Hf_{0.5}Fe_{0.5}Ni_{0.5}Sb$> $Ti_{0.5}Hf_{0.5}Fe_{0.33}Co_{0.33}Ni_{0.33}Sb$, with $Ti_{0.5}Hf_{0.5}Fe_{0.33}Co_{0.33}Ni_{0.33}Sb$ possessing a κ_L of 1.8 $Wm^{-1}K^{-1}$, at T = 973 K.
- $Ti_{0.5}Hf_{0.5}Fe_{0.33}Co_{0.33}Ni_{0.33}Sb$ is n-type, unlike the preceding samples that were p-type. Concomitantly, the bipolarity in the S is not observed in the measurement range (298 K − 973 K).

Actual chemical formula	Expanded chemical formula	Sign of Seebeck
$TiFe_{0.5}Ni_{0.5}Sb$	$Ti_2FeNiSb_2$	+ve (With bipolarity)
$HfFe_{0.5}Ni_{0.5}Sb$	$Hf_2FeNiSb_2$	+ve (With bipolarity)
$Ti_{0.5}Hf_{0.5}Fe_{0.5}Ni_{0.5}Sb$	$TiHfFeNiSb_2$	+ve (With bipolarity)
$Ti_{0.5}Hf_{0.5}Fe_{0.33}Co_{0.33}Ni_{0.33}Sb$	$Ti_{1.5}Hf_{1.5}FeCoNiSb_3$	-ve (Without bipolarity)

Table 3.1: Table of alloys synthesized in Phase -I

From phase I, $Ti_{0.5}Hf_{0.5}Fe_{0.33}Co_{0.33}Ni_{0.33}Sb$ was observed to be an advantageous primary sample, with the lowest κ_L and the absence of bipolarity in Seebeck coefficient in the working range. Therefore, phase II was initiated to synthesize p-type and n-type samples based on the same and enhance the electrical conductivities.

3.2 Phase - II : Enhancement of Electronic Properties

The possibility of the synthesis of p-type and n-type counterparts from the aforesaid parental original alloy (which is preferred with device fabrication in mind) was embarked upon in this phase. As mentioned earlier, the availability of internal tuning of the Fe-Ni ratio to synthesize p-type and n-type counterparts was capitalized. They were prepared by weighing the elements in appropriate amounts, arc melting, and hot pressing. Their XRD plots are shown in Figure 3.2.1.

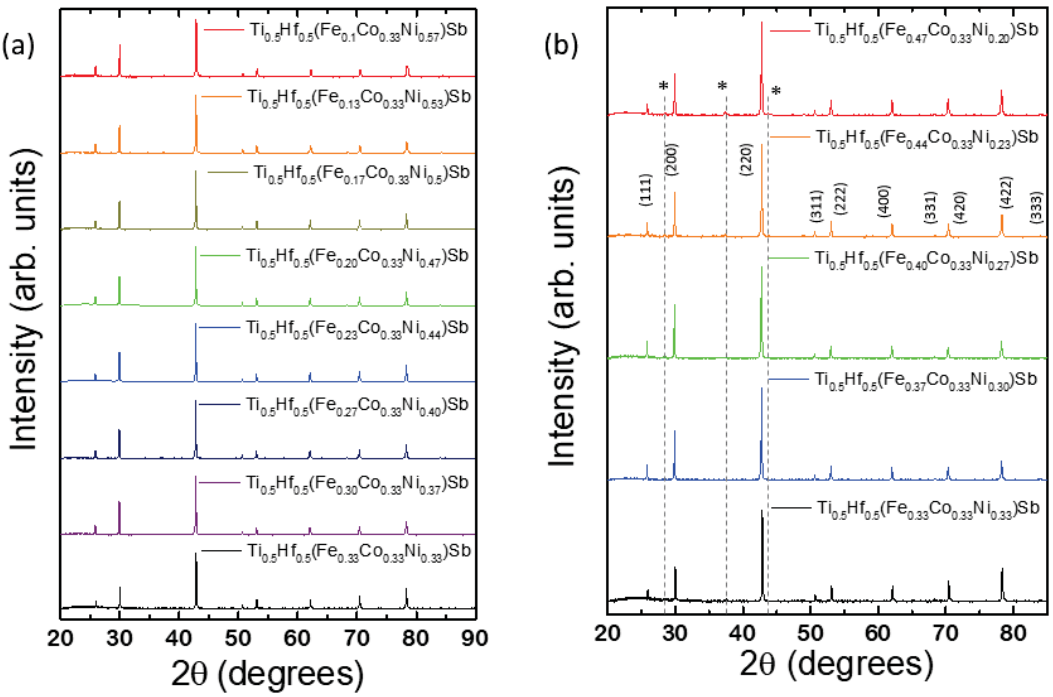

Figure 3.2.1: XRD data of (a) Ni-rich series and (b) Fe-rich series (* denote the HfFe peaks)

The samples are found to possess high configurational entropies (defined as $-k_B \sum_{i=1}^{N} w_i ln(w_i)$, where w_i is the fraction of each element at each site and N is the number of sites, which is 3 here) [19]. The configurational entropies of the samples are shown in Figure 3.2.2. It can be noted that the alloys' configurational entropy values are all above $1.5R$. The samples were predominantly pure and single-phased, except in the cases of Fe-rich counterparts, where tiny impurity peaks of HfFe are observed (which are facilitated by the increase in Fe

proportion). Due to this observation of the enhancement of impurity phases, the maximum Fe-rich sample in our study is $Ti_{0.5}Hf_{0.5}Fe_{0.47}Co_{0.33}Ni_{0.2}Sb$ (This is by when the $\frac{Fe}{Ni}$ ratio has gone from 1 to 2.33 i.e. $\frac{10}{10} \rightarrow \frac{14}{6}$). On the other hand, on the Fe-deficient side, when the Fe-Ni imbalance increases even more, resulting in the entropy being lesser than $1.7R$ and VEC moving even further away from 18, we observe the double-phased peaks (beyond the $Ti_{0.5}Hf_{0.5}Fe_{0.17}Co_{0.33}Ni_{0.5}Sb$ sample).

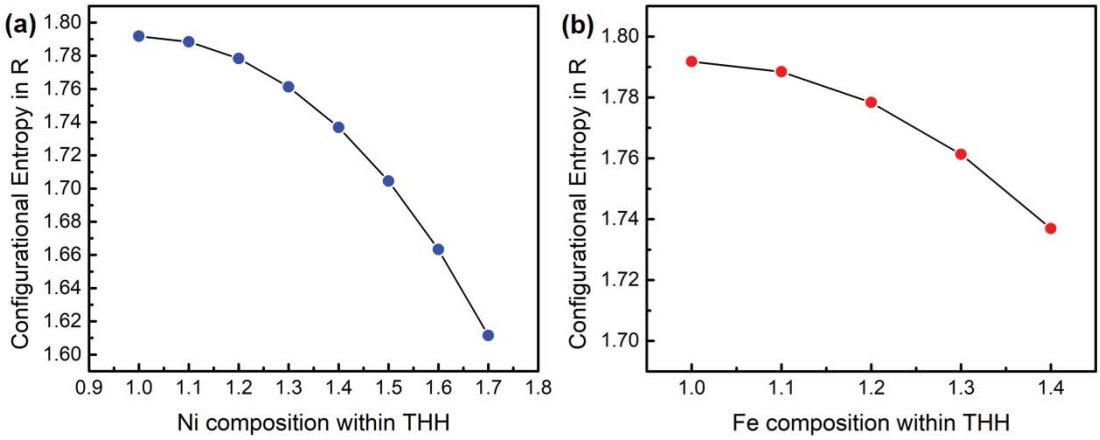

Figure 3.2.2: The configurational entropies of (a) Ni-rich series and (b) Fe-rich series (x-axis of (a) denotes the proportion of the Ni at the Y-site out of 3, with Fe being decreased correspondingly, and similarly for (b) increasing Fe proportion is shown)

The investigation of the n-type series was done in collaboration with a PhD student, Ankit Kumar, and therefore shall not be discussed further in this study whereas the p-type series is investigated with regard to this study. With regards to the comparison of the thermoelectric properties, since the most Fe-rich composition is $Ti_{0.5}Hf_{0.5}Fe_{0.47}Co_{0.33}Ni_{0.2}Sb$, the corresponding most Ni-rich (n-type) against which the inferences shall be made is $Ti_{0.5}Hf_{0.5}Fe_{0.2}Co_{0.33}Ni_{0.47}Sb$.

The lattice parameters calculated for the p-type alloys are depicted in Figure 3.2.3. We can observe that the lattice parameters increase with the increase in Fe proportion and the corresponding decrease in Ni proportion as Fe has a greater atomic radius and thus is expected to result in the enlargement of the lattice.

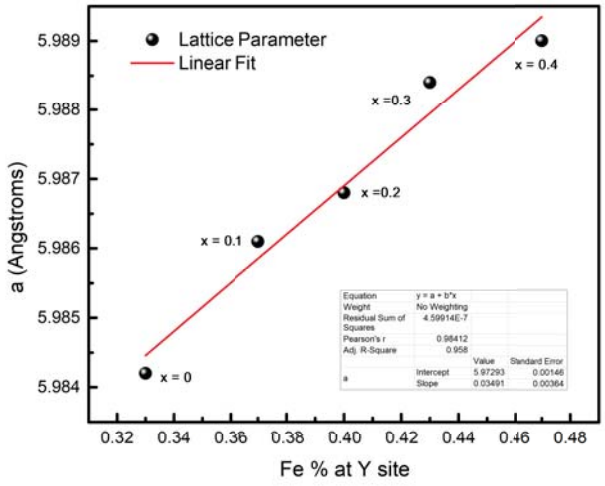

Figure 3.2.3: Lattice parameters of Fe-rich THH ($Ti_{1.5}Hf_{1.5}Fe_{1+x}CoNi_{1-x}Sb_3$, expressed in expanded formula)

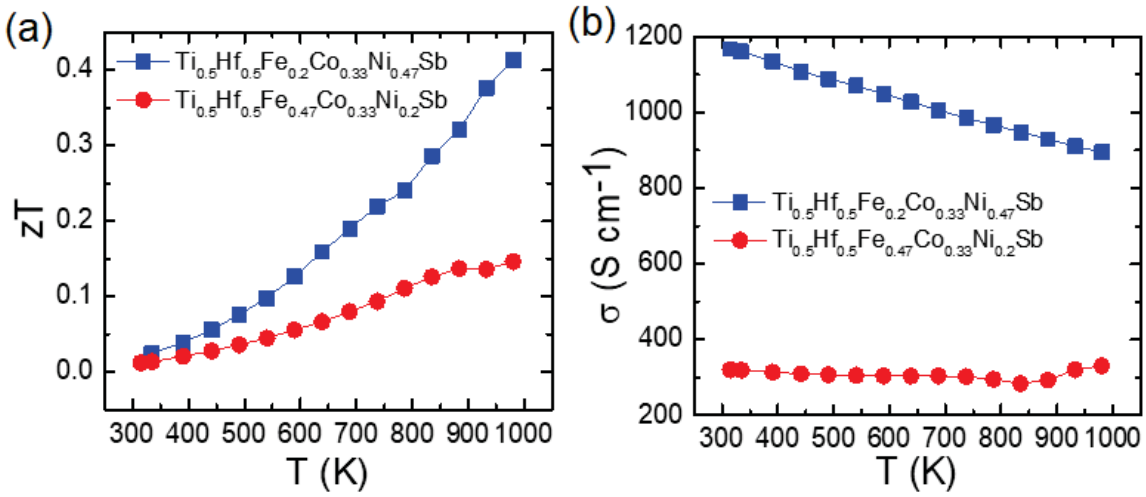

Figure 3.2.4: Comparison of the extreme p-type and n-type counterparts: (a) zT and (b) electrical conductivity

The Seebeck and resistivity measurements that were performed on the LSR-3 setup showcase a glaring inequality in the values of properties obtained for equivalent p-type and n-type

counterparts. The zT, calculated with the thermal conductivities obtained from the LFA setup, of $Ti_{0.5}Hf_{0.5}Fe_{0.2}Co_{0.33}Ni_{0.47}Sb$ is 0.4 at 973 K whereas the p-type counterpart, with identical doping proportion, $Ti_{0.5}Hf_{0.5}Fe_{0.47}Co_{0.33}Ni_{0.2}Sb$ has a zT of 0.14 at the same temperature (973 K), as seen in Figure 3.2.4.(a). Looking at the individual properties, the reason for this dissimilarity is primarily due to the difference in their σ, as shown in Figure 3.2.4.(b).

Therefore, raising the zT of the p-type counterpart became the problem at hand. This was the challenge to be tackled; as for device fabrication, the two legs (p-type and n-type) must have similar physical properties and high enough zT for its efficiency to be good enough for considerable thermoelectric performance.

To summarize phase II,

- Both n-type and p-type series of $Ti_{0.5}Hf_{0.5}Fe_{0.33+x}Co_{0.33}Ni_{0.33-x}Sb$ were synthesized by counterbalancing the $\frac{Fe}{Ni}$ ratio (p-type (x>0) by $\frac{10}{10} \rightarrow \frac{14}{6}$ and n-type (x<0) by $\frac{10}{10} \rightarrow \frac{5}{15}$)
- The measured zT value of n-type was higher than the corresponding p-type (0.4 and 0.14 at 973 K respectively)
- The variation can be clearly seen to have arisen from their corresponding electrical conductivities.

Actual chemical formula	Expanded chemical formula	Sign of Seebeck
$Ti_{0.5}Hf_{0.5}Fe_{0.17}Co_{0.33}Ni_{0.5}Sb$	$Ti_{1.5}Hf_{1.5}Fe_{0.5}CoNi_{1.5}Sb_3$	-ve
$Ti_{0.5}Hf_{0.5}Fe_{0.2}Co_{0.33}Ni_{0.47}Sb$	$Ti_{1.5}Hf_{1.5}Fe_{0.6}CoNi_{1.4}Sb_3$	-ve
$Ti_{0.5}Hf_{0.5}Fe_{0.23}Co_{0.33}Ni_{0.44}Sb$	$Ti_{1.5}Hf_{1.5}Fe_{0.7}CoNi_{1.3}Sb_3$	-ve
$Ti_{0.5}Hf_{0.5}Fe_{0.27}Co_{0.33}Ni_{0.4}Sb$	$Ti_{1.5}Hf_{1.5}Fe_{0.8}CoNi_{1.2}Sb_3$	-ve
$Ti_{0.5}Hf_{0.5}Fe_{0.3}Co_{0.33}Ni_{0.37}Sb$	$Ti_{1.5}Hf_{1.5}Fe_{0.9}CoNi_{1.1}Sb_3$	-ve
$Ti_{0.5}Hf_{0.5}Fe_{0.33}Co_{0.33}Ni_{0.33}Sb$	$Ti_{1.5}Hf_{1.5}FeCoNiSb_3$	-ve
$Ti_{0.5}Hf_{0.5}Fe_{0.37}Co_{0.33}Ni_{0.3}Sb$	$Ti_{1.5}Hf_{1.5}Fe_{1.1}CoNi_{0.9}Sb_3$	+ve
$Ti_{0.5}Hf_{0.5}Fe_{0.4}Co_{0.33}Ni_{0.27}Sb$	$Ti_{1.5}Hf_{1.5}Fe_{1.2}CoNi_{0.8}Sb_3$	+ve
$Ti_{0.5}Hf_{0.5}Fe_{0.44}Co_{0.33}Ni_{0.23}Sb$	$Ti_{1.5}Hf_{1.5}Fe_{1.3}CoNi_{0.7}Sb_3$	+ve
$Ti_{0.5}Hf_{0.5}Fe_{0.47}Co_{0.33}Ni_{0.2}Sb$	$Ti_{1.5}Hf_{1.5}Fe_{1.4}CoNi_{0.6}Sb_3$	+ve

Table 3.2: Table of alloys synthesized in Phase -II

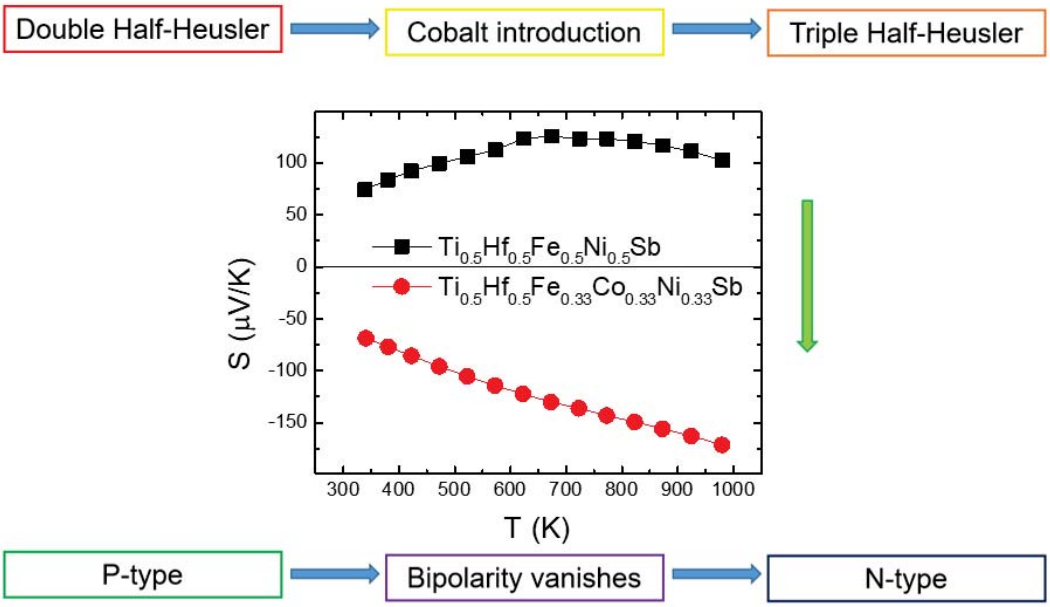

Figure 3.2.5: The effects of Co introduction: "The p-type puzzle"

This is where we take into consideration the previous observation of the fact that the introduction of Co into the Y-site had transformed the compound into an intrinsically n-type material. This should have led to the favouring of better n-type properties than the p-type upon similar tuning of the Y-site. Therefore, in an attempt to retain the removal of bipolarity while also aiming to upgrade the p-type properties, I initiated a new investigation aimed at systematically decreasing the Cobalt concentration, which brings us to the Phase III of this project, presented next.

3.3 Phase - III : Decreasing Cobalt Concentration

In this phase, the aim was to improve the p-type counterpart's zT. Since the primary reason for low zT was identified as poor electrical conductivity, the goal was to raise the same. The idea to enhance the p-type was to therefore fix $\frac{\text{Fe}}{\text{Ni}}$ ratio at its extreme value 2.33 and to progressively decrease Co concentration alone. This direction was undertaken due to the observation that the Co introduction had transformed the compound into an intrinsically n-type material, as mentioned before. The pristine counterparts, where $\frac{\text{Fe}}{\text{Ni}}$ at 1 were also synthesized.

The materials were synthesized by taking appropriate amounts of the elemental composition, arc melting, and hot pressing. The XRDs are shown in Figure 3.3.1. Here we see that the pristine counterparts are clearly single-phase, whereas the Fe-rich possess the impurity peaks (the HfFe peaks). One can observe a slight enhancement of the HfFe peaks over the successive reduction of the Co proportion, which will be looked into in the following discussions.

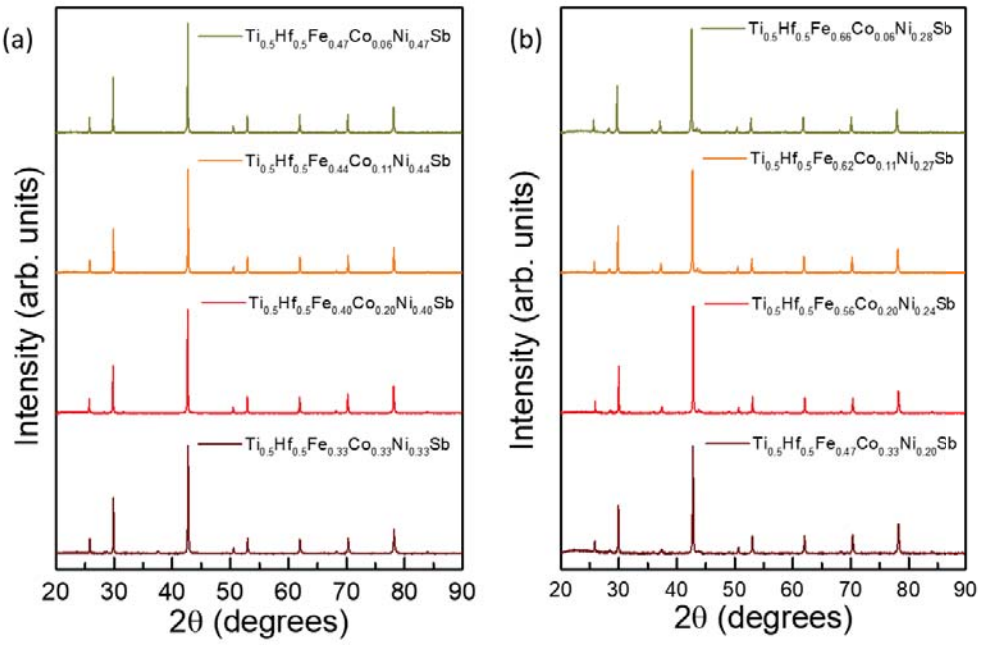

Figure 3.3.1: XRD data of (a) Pristine Co-decreased THH and (b) Fe-rich Co-decreased THH

The LSR and LFA measurements were performed on the samples. The Fe-rich series with Co concentration progressively decreasing turned out to follow the intuition. The Seebeck, conductivity, PF, and weighted mobility plots are shown in Figure 3.3.2. The electrical conductivities are promisingly vindicating the expectations. As Co concentration decreases from 33% at Y-site to 20%, 11%, and 6%, (with $\frac{\text{Fe}}{\text{Ni}}$ still at 2.33, as mentioned earlier) σ successively increases.

An interesting observation is that the Seebeck coefficient did not drop (in fact showed a slight increase) down to Co-11% at Y-site, but dropped considerably for the next sample Co-6% at Y-site indicating that the optimal Co-doping lies between 11% and 6%. This is unexpected usually as the S is inversely correlated to the carrier concentration (n), while σ is proportionately dependent on the same, and the increase in conductivity is either by the increase in n or in μ. We delve into this further in the next paragraph where we discuss the weighted mobility of these alloys. This resulted in the power factors steadily increasing from Co-33% till Co-11% and decreasing slightly for Co-6%.

Weighted mobility, another way of comparing the materials' thermoelectric properties, is defined as $\mu_W = \mu_o(\frac{m^*}{m_e})^{\frac{3}{2}}$, where μ_o is the intrinsic regime's peak mobility for the material. This weighted mobility can be procured using the S, resistivity, and temperature by the following formula [20]:

$$\mu_W = \frac{3h^3}{8\pi e(2m_e k_B T)^{3/2}\rho} \times \left[\frac{exp[\frac{|S|}{k_B/e} - 2]}{1 + exp[-5(\frac{|S|}{k_B/e} - 1)]} + \frac{\frac{3|S|}{\pi^2 k_B/e}}{1 + exp[5(\frac{|S|}{k_B/e} - 1)]} \right]$$

which can be further simplified as,

$$\mu_W = 331\frac{cm^2}{Vs}\big(\frac{1}{\rho(\mu\Omega m)}\big)\big(\frac{T(K)}{300}\big)^{-3/2} \left[\frac{exp[\frac{|S|}{k_B/e} - 2]}{1 + exp[-5(\frac{|S|}{k_B/e} - 1)]} + \frac{\frac{3|S|}{\pi^2 k_B/e}}{1 + exp[5(\frac{|S|}{k_B/e} - 1)]} \right]$$

It can be seen from Figure 3.3.2 (d), the weighted mobilities of Co-11% and Co-6% samples are the highest, with clear jumps from the previous two upon successive decrease in Cobalt

concentration at Y-site, and Co-11% sample is a tad better at higher temperatures. This, with the resultant high PF of the Co-11% sample, makes it the most favourably optimized sample from the point of the electronic properties.

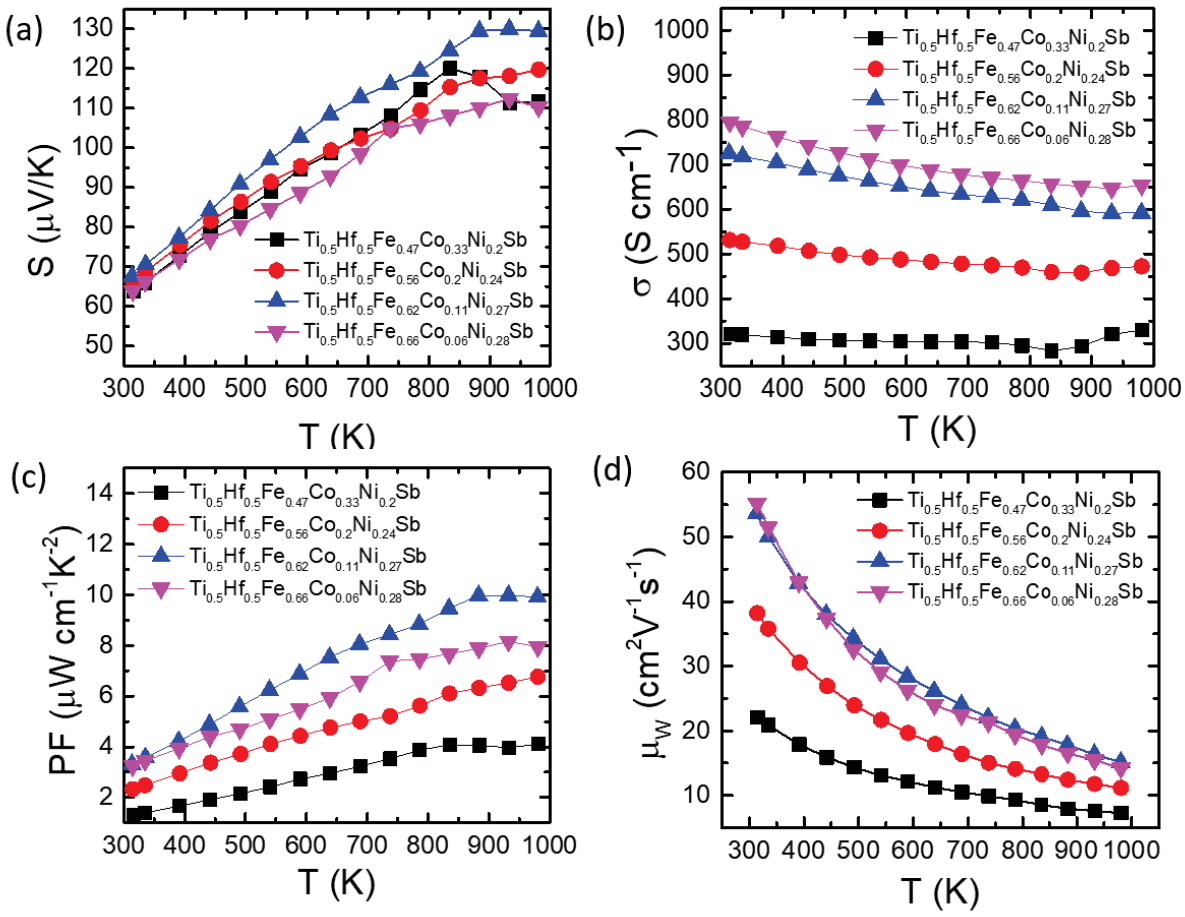

Figure 3.3.2: (a) The Seebeck coefficients, (b) Electrical conductivities, (c) Power Factors and (d) Weighted mobilities of the decreased Cobalt series (With $\frac{\text{Fe}}{\text{Ni}} = 2.33$ and Co % at Y-site going from $33, 20, 11,$ till 6)

The total thermal conductivities, electronic parts, lattice parts, and the zT are shown in Figure 3.3.3. The disordered κ_{Total} can be understood by analyzing the individual parts. The κ_e is calculated, as previously mentioned, from the Wiedemann-Franz law ($\kappa_e = L$), where the Lorenz number for doped semiconductors is calculated from the equation $L = 1.5 + exp(\frac{-|S|}{116})$ [7]. From Figure 3.3.3 (b), we see the trend in κ_e clearly: With increasing σ,

the κ_e increases, and due to the direct relation to temperature, κ_e rises with T. This gives us the κ_L ($\kappa_{Total} - \kappa_e$) as shown in Figure 3.3.3 (c). With this κ_{Total} observed for all of them, the previously identified favourable sample Co-11% has a low enough value such that its zT still ended up being the maximum - 0.32 - as shown in Figure 3.3.3 (d). This is a significant increase from an initial zT of 0.14 in the case of Co-33%: about 230% the original zT. This is comparable to the n-type $Ti_{0.5}Hf_{0.5}Fe_{0.2}Co_{0.33}Ni_{0.47}Sb$, whose zT is 0.40.

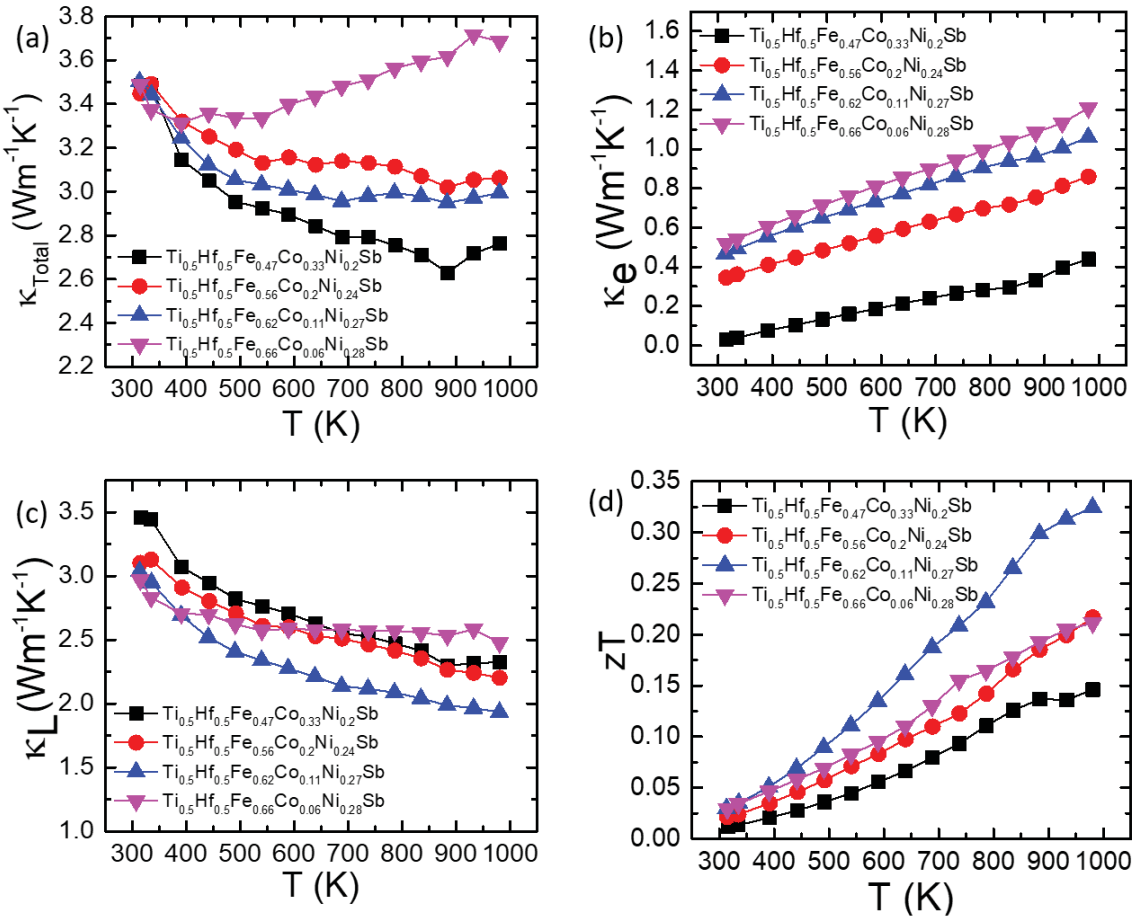

Figure 3.3.3: (a) The κ_{Total}, (b) κ_e (electronic part), (c) κ_L (lattice part) and (d) zT of the decreased Cobalt series

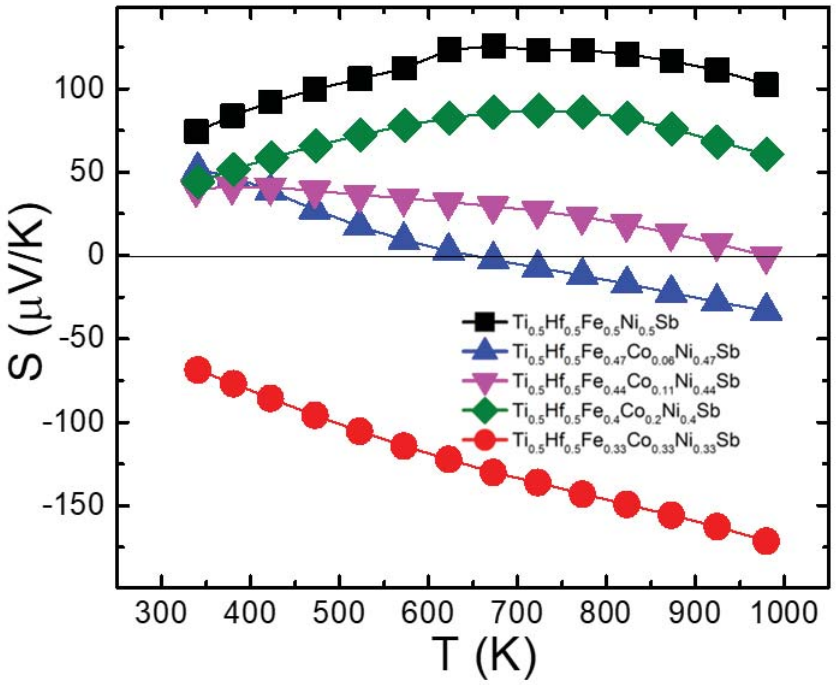

Figure 3.3.4: Seebeck coefficients of the pristine Co-decreased series ($\frac{\text{Fe}}{\text{Ni}} = 1$ and Co % at Y-site going from $33, 20, 11$, till 6)

The Seebeck coefficients of the pristine Co-reduced series verify the intuition. One can see from Figure 3.3.4, the gradual shift from the n-type to the p-type regime. At the same time, the recurrence of bipolarity is seen in the case of Co-6%. This vindicates the presumptions in the previous sections of the discussions that the Co introduction had while widening the bandgap, also pushed the material into n-type regime. Therefore, along with the power factor and weighted mobilities data, this too suggests the preference of Co-11% to be the prospective sample for the p-type regime.

Now, the reason for conductivity needs to be analyzed. It was already noted in the XRD that the impurity phases associated with Fe-richness were also slightly enhancing. It can be clearly seen that the decrease in the concentration of Co has thereby resulted in an increase in proportion to the amount of Fe per formula unit (which also explains the increase in the prominence of the impurity peaks) and has resulted in subsequently lower VECs, hence

higher hole-doping (From 27% hole-doping for the case of Co-33% to 32% for Co-20%, 35% for Co-11%, and 38% for Co-6%, as shown in Table 3.3). This can also be seen in the increase in the lattice parameters extracted from the XRD data, as plotted in Figure 3.3.5. The steady increase showcases the greater Fe composition.

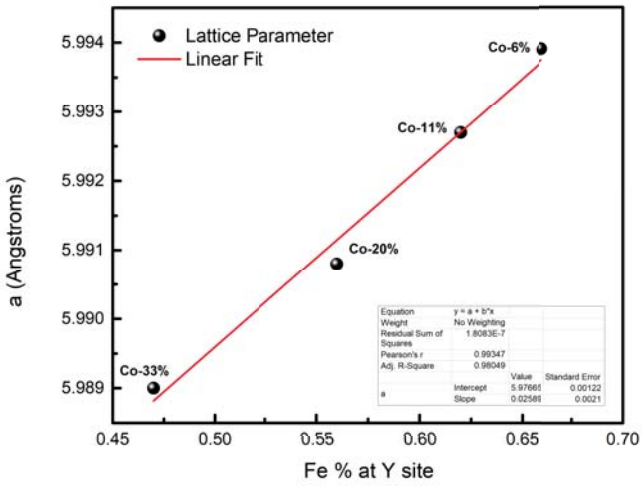

Figure 3.3.5: Lattice parameters of decreased Cobalt THH series ($\frac{\text{Fe}}{\text{Ni}} = 2.33$)

To summarize phase III,

- The successive decrease in the Co concentration, with $\frac{\text{Fe}}{\text{Ni}} = 2.33$ resulted in a progressive increase in the electrical conductivity
- The PF continued to go up till Co-11% at the Y-site after which it dropped; The decrease from Co-11% to Co-6% is due to the decrease in the Seebeck coefficient
- The increase in the weighted mobilities upon the decrease in concentration is responsible for the increase in the electrical conductivity
- The decrease in the Co concentration has successively pushed the materials to favour the p-type behaviour (VEC < 18), while at the same time, it has also led to a reduction in the bandgap

- The zT increased from 0.14 at 973 K for $Ti_{0.5}Hf_{0.5}Fe_{0.47}Co_{0.33}Ni_{0.2}Sb$ to 0.32 for $Ti_{0.5}Hf_{0.5}Fe_{0.62}Co_{0.11}Ni_{0.27}Sb$ at the same temperature (973 K), which is comparable to the corresponding n-type counterpart's $zT = 0.40$.

Actual chemical formula	Expanded chemical formula	VEC	Sign of Seebeck
$Ti_{0.5}Hf_{0.5}Fe_{0.47}Co_{0.33}Ni_{0.2}Sb$	$Ti_{1.5}Hf_{1.5}Fe_{1.4}CoNi_{0.6}Sb_3$	17.73	+ve
$Ti_{0.5}Hf_{0.5}Fe_{0.56}Co_{0.2}Ni_{0.24}Sb$	$Ti_{1.25}Hf_{1.25}Fe_{1.4}Co_{0.5}Ni_{0.6}Sb_{2.5}$	17.68	+ve
$Ti_{0.5}Hf_{0.5}Fe_{0.62}Co_{0.11}Ni_{0.27}Sb$	$Ti_{1.125}Hf_{1.125}Fe_{1.4}Co_{0.25}Ni_{0.6}Sb_{2.25}$	17.65	+ve
$Ti_{0.5}Hf_{0.5}Fe_{0.66}Co_{0.06}Ni_{0.28}Sb$	$Ti_{1.06}Hf_{1.06}Fe_{1.4}Co_{0.12}Ni_{0.6}Sb_{2.12}$	17.62	+ve

Table 3.3: Table of alloys synthesized in Phase -III

3.4 Phase - IV : Doping the Cobalt-decreased samples

The Fe-rich series with decrease in Co-concentration possess the HfFe impurity phases, evident from their XRDs, whereas the pristine Co-reduced series is phase pure, as seen from their clean XRD data. It is desirable for the samples to be phase pure for the impurity phases could be potential disruptors of the preferred physical properties of the sample and to be the mark of the ensured reproducibility of the sample.

This, along with the intention to further amplify the thermoelectric properties of the materials, prompted further investigation involving doping with Sn at the Sb-site (Z-site) (10% and 20%) and Y at TiHf-site (X-site) (10%) in the sample for the Pristine Co-11% sample, i.e. with $\frac{\text{Fe}}{\text{Ni}} = 1 : (\text{Ti}_{0.5}\text{Hf}_{0.5}\text{Fe}_{0.44}\text{Co}_{0.11}\text{Ni}_{0.44}\text{Sb})$.

The samples were synthesized by weighing precursors in appropriate amounts, in their elemental form, arc melted, and hot pressed. The XRD data are shown in Figure 3.4.1. The Sn-doped samples were phase pure. The Y-doped sample was found to have YSb impurity phases, which remained after hot-press sintering at 1100 °C, as shown in Figure 3.4.1.

This series ended up with much lower conductivities (~ 100 Scm^{-1} for the Y-doped sample and even lower for the Sn-doped samples, as from their LSR data (at room temperature)). Therefore, this external doping route was not focused on beyond this phase.

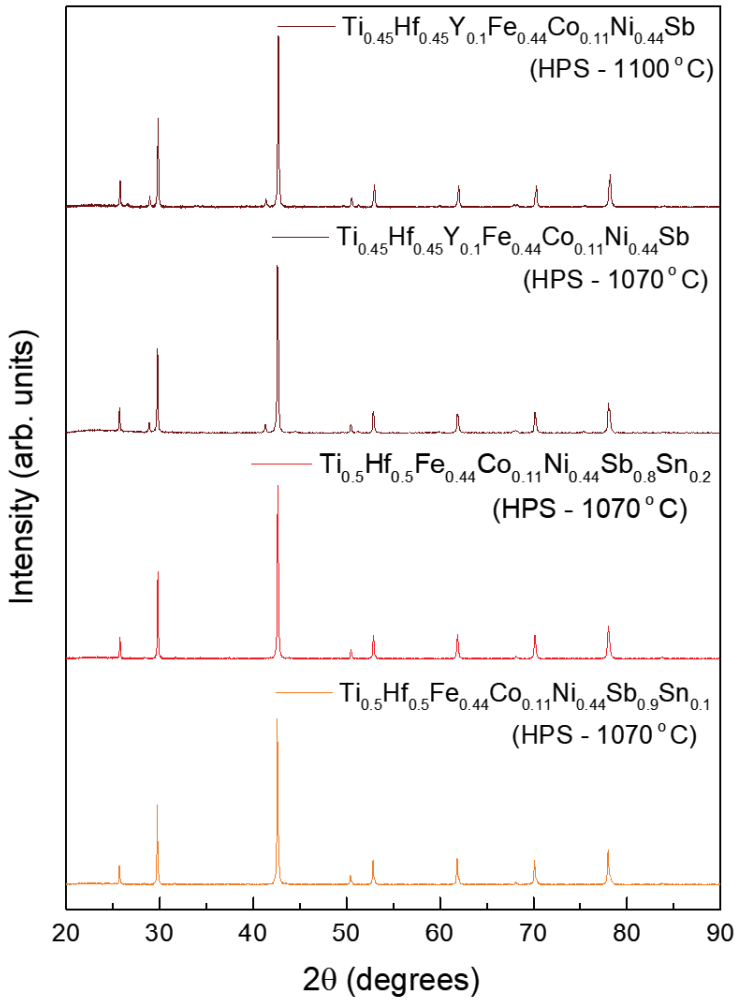

Figure 3.4.1: XRD data of the doped series

3.5 Phase - V : Annealing the Co-decreased samples

The other route investigated was to get rid of the impurity phases from the sample - $Ti_{0.5}Hf_{0.5}Fe_{0.62}Co_{0.11}Ni_{0.27}Sb$. This was carried out by annealing. Quartz tubes are preheated at 900 °C for 24 hours to eradicate any trace amounts of water that might be present on the interior surfaces of the same. The sample (hot pressed and cut pieces, covered with Boron Nitride spray to prevent reacting with the quartz wall) was loaded into a preheated quartz tube carefully and vacuumed to reach the order of 10^{-4} mbar. This tube was loaded onto a box furnace and was raised to a temperature of 900 °C from room temperature by ramping for 10 hours and maintained there for seven days. This is followed by the sudden quenching of the same in a container of ice water by the end of the process. The temperature profile is shown in Figure 3.5.1.(a).

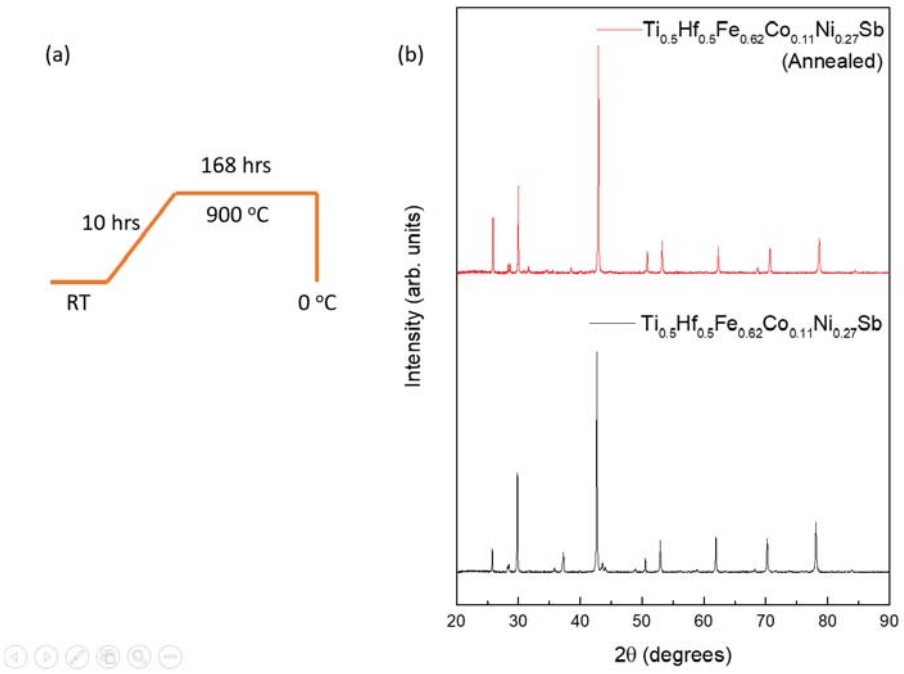

Figure 3.5.1: (a) The temperature profile of annealing the sample and (b) the XRD data of the sample

The XRD data is shown in Figure 3.5.1.(b). The annealed sample shows improvement to a certain degree in certain phases but also a slight enhancement of a previously non-prominent

impurity peak. Further treatment at higher temperatures could aid in the removal of the impurity phases, provided they're not the most stable phases in that regime too.

Chapter 4

Conclusion

The initial part of the thesis focused on the minimizing of the κ_L of the half-Heusler system by alloying and synthesizing the so-called double and triple half-Heuslers, to reach a minimal κ_L of 1.8 $Wm^{-1}K^{-1}$ at 973 K for the THH $Ti_{0.5}Hf_{0.5}Fe_{0.33}Co_{0.33}Ni_{0.33}Sb$.

This was followed by the generation of the p-type and n-type series from the aforementioned parental alloy via tuning Fe-Ni ratio. This led to the observation of comparatively superior properties of n-type over p-type, potentially arising from the fact that Co introduction into the DHH alloy to make it $Ti_{0.5}Hf_{0.5}Fe_{0.33}Co_{0.33}Ni_{0.33}Sb$ had inherently pushed it to favour the n-type. This is evident from the conductivity of n-type being several times higher than that of the p-type, leading to $Ti_{0.5}Hf_{0.5}Fe_{0.20}Co_{0.33}Ni_{0.47}Sb$ having a $zT = 0.40$ at 973 K, as opposed to the corresponding p-type's ($Ti_{0.5}Hf_{0.5}Fe_{0.47}Co_{0.33}Ni_{0.20}Sb$) zT being 0.14 at 973 K.

This led to us progressively decreasing the Co concentration in the material (decreasing the Co concentration while maintaining $\frac{Fe}{Ni} = 2.33$ in all of them), resulting in significant improvement in the zT of a new p-type HH material. The impressive increase in the electrical conductivities upon decreasing the Co concentration, without the Seebeck coefficient diminishing (up until Co-6%, where it did), resulted in a $zT = 0.32$ for the Co-11% sample, that is $Ti_{0.5}Hf_{0.5}Fe_{0.62}Co_{0.11}Ni_{0.27}Sb$. The pristine series ($\frac{Fe}{Ni} = 1$, i.e. Fe:Ni::1:1) with Co-reduced were also synthesized and measured to observe the Seebeck coefficient variance with

the Co-proportion in the materials, which verified the initial intuition of Co introduction widening the bandgap, removing the bipolarity, and also pushing the material into intrinsic n-type.

Further dopants (Sn at Z-site and Y at X-site) were experimented with; however, this resulted in a marked decrease in the conductivities. Thus, the extrinsic doping route was not explored further. Annealing the samples to remove HfFe impurity phases was performed. While this did help in reducing the intensity of some of the impurity peaks in the powder x-ray diffraction, some new impurity peaks, that were not there before annealing, appeared in the XRD pattern, indicating the suppression of the original secondary phase, but the appearance of new secondary phases; this rendered this exercises ineffective. Perhaps, changing the annealing conditions may help in overcoming these issues.

In summary, in this thesis we attempted to broaden the purview of half-Heusler systems by investigating some new and previously unreported DHH and THH systems, in the attempts to lower the lattice thermal conductivity, thereby overcoming the primary challenge plaguing the HH systems. Once the "p-type puzzle" was encountered, the study utilized a novel approach, wherein the Co concentration is systematically reduced to enhance the power factor (thereby bringing p-type zT comparable to that of the n-type). In future, we plan to measure the carrier concentration of these alloys (Co-decreased with $\frac{\text{Fe}}{\text{Ni}} = 2.33$) to understand how the Hall mobility and carrier concentration varies across the series. This can help us shed light on the mechanism leading to a remarkable increase in the electrical conductivity upon the decrease in the Co concentration.

Bibliography

[1] C. Forman, I. K. Muritala, R. Pardemann, and B. Meyer, Estimating the global waste heat potential, Renewable and Sustainable Energy Reviews, Volume 57, Pages 1568-1579 (2016)

[2] J. R. Sootsman, D. Y. Chung , and M. G. Kanatzidis, New and Old Concepts in Thermoelectric Materials, Angewandte Chemie International Edition, Volume 48, Issue 46 (2009)

[3] S. Chen, and Z. Ren, Recent progress of half-Heusler for moderate temperature thermoelectric applications, Materials Today, Volume 16, Issue 10, Pages 387-395, ISSN 1369-7021 (2013)

[4] H. Goldsmid, Introduction to Thermoelectricity, Springer Series in Materials Science, Springer Berlin Heidelberg, ISBN 9783642007163 (2009)

[5] Snyder, G., and Toberer, E., Complex thermoelectric materials. Nature Mater 7, 105–114 (2008)

[6] Kurosaki, K., Takagiwa, Y., and Shi, X., Thermoelectric Materials: Principles and Concepts for Enhanced Properties, Berlin, Boston: De Gruyter (2020)

[7] H. Kim, Z. M. Gibbs, Y. Tang, H. Wang, and G. J. Snyder, Characterization of Lorenz number with Seebeck coefficient measurement, APL Mater, 3 (4): 041506 (2015)

[8] Li, J., Chen, Z., Zhang, X., Yu, H., Wu, Z., Xie, H., Chen, Y., and Pei, Y., Simultaneous Optimization of Carrier Concentration and Alloy Scattering for Ultrahigh Performance GeTe Thermoelectrics. Advanced Science, 4(12), 1700341, (2017)

[9] D. Wang, X. Li, and H. Sun, Modulation Doping: A Strategy for 2D Materials Electronics, Nano Lett., 21, 14, 6298–6303 (2021)

[10] B. Yu, M. Zebarjadi, H. Wang, K. Lukas, H. Wang, D. Wang, C. Opeil, M. Dresselhaus, G. Chen, and Z. Ren, Enhancement of Thermoelectric Properties by Modulation-Doping in Silicon Germanium Alloy Nanocomposites, Nano Lett., 12, 4, 2077–2082 (2012)

[11] L. Chen, Y. Liu, J. He, T. M. Tritt, and S. J. Poon, High thermoelectric figure of merit by resonant dopant in half-Heusler alloys, AIP Advances, 7 (6): 065208 (2017)

[12] W. Liu, X. Tan, K. Yin, H. Liu, X. Tang, J. Shi, Q. Zhang, and C. Uher, Convergence of Conduction Bands as a Means of Enhancing Thermoelectric Performance of n-Type Mg2Si1-xSnx Solid Solutions, Phys. Rev. Lett, 108, 166601 (2012)

[13] C. Gayner, and Y. Amouyal, Energy Filtering of Charge Carriers: Current Trends, Challenges, and Prospects for Thermoelectric Materials, Advanced Functional Materials, 30(18), 1901789, (2020)

[14] Yu, J., Fu, C., Liu, Y., Xia, K., Aydemir, U., Chasapis, T. C., Snyder, G. J., Zhao, X., and Zhu, T., Unique Role of Refractory Ta Alloying in Enhancing the Figure of Merit of NbFeSb Thermoelectric Materials, Advanced Energy Materials, 8(1), 1701313,(2017)

[15] A. J. Minnich, M. S. Dresselhaus, Z. F. Ren, and G. Chen, Bulk nanostructured thermoelectric materials: current research and future prospects, Energy Environ. Sci., 2, 466-479 (2009)

[16] T. Graf, C. Felser, and S. S. P. Parkin, Simple rules for the understanding of Heusler compounds, Progress in Solid State Chemistry, Volume 39, Issue 1, Pages 1-50, ISSN 0079-6786 (2011)

[17] Shashwat Anand, Max Wood, Yi Xia, Chris Wolverton, and G. Jeffrey Snyder, Double Half-Heuslers, Joule, Volume 3, Issue 5 (2019)

[18] T. Sekimoto, K. Kurosaki, H. Muta and S. Yamasaka, Thermoelectric and thermophysical properties of TiCoSb, ZrCoSb, HfCoSb prepared by SPS, Materials Transactions, Vol. 47, No. 6 pp. 1445 to 1448 (2006)

[19] Li, M., Cao, G., Luo, Y., Sheng,C., and Liu,H., Predicting the lattice thermal conductivity of alloyed compounds from the perspective of configurational entropy. npj Comput Mater 8, 75 (2022)

[20] Snyder, G. J., Snyder, A. H., Wood, M., Gurunathan, R., Snyder, B. H., and Niu, C., Weighted Mobility. Advanced Materials, 32(25), 2001537 (2020)